Chapter VII

FIRST-WALL AND LIMITER SYSTEMS

M.A. ABDOU	–	USA
G. CASINI	–	Euratom
T. HIRAOKA	–	Japan
T. KOBAYASHI	–	Japan
G.L. KULCINSKI	–	USA
D. LEGER	–	Euratom
P. SCHILLER	–	Euratom
D.V. SEREBRENNIKOV	–	USSR
G.E. SHATALOV	–	USSR
D.L. SMITH	–	USA

1. DESCRIPTION AND OPERATING CONDITIONS

The design and performance of the first wall received considerable attention in the INTOR studies. Several options were proposed and key issues were treated in considerable detail. The analyses performed during Phase One are documented in Refs [2 – 5]. Additional information on the materials data base assessment is given in the Phase-Zero report [1]. Chapter VII describes the design concept and performance characteristics of the reference design of the first wall, which is a bare stainless steel wall. A back-up design, which is similar to the reference design but uses radiatively cooled graphite tiles on the inboard wall, is also briefly described. A summary of the work on an alternative aluminium first-wall design is given in Section XXI.5.

The first-wall system as defined in the present study, which consists of the plasma chamber and serves as the first physical barrier for the plasma, has the following components:

(a) An outboard wall which serves as the major part of the plasma chamber surface and receives particle and radiation heat loads from the plasma and radiative heating from the divertor
(b) An inboard wall which receives radiative and particle flux during plasma burn and the major fraction of the plasma energy during a disruption
(c) A limiter region on the outboard wall which forms the plasma edge during the early part of start-up
(d) A beam shine-through region on the inboard wall which receives neutral beam shine-through at the beginning of neutral injection
(e) A ripple armour on the outboard wall which receives enhanced particle fluxes caused by ripple effects during the late stages of neutral injection.

TABLE VII-1. OPERATING SCENARIO FOR INTOR

	Availability (%)	Cycle time (s)	Burn time (s)	Number of shots	Number of disruptions	Neutron fluence (n/m^2)
Stage 1						
(a) Year 1	10	3.2×10^6	2.3×10^6	2.2×10^4	115	—
(b) Years 2, 3	15	9.4×10^6	6.8×10^6	6.6×10^4	340	3.6×10^{25}
Stage 2						
Per year	25	7.9×10^6	6.3×10^6	3.1×10^4	31	3.2×10^{25}
Years 4–7	25	31.6×10^6	25.2×10^6	12.4×10^4	124	12.8×10^{25}
Stage 3						
Per year	50	15.8×10^6	12.6×10^6	6.2×10^4	63	6.4×10^{25}
Years 8–15	50	126.0×10^6	101.0×10^6	49.6×10^4	504	51.2×10^{25}
Lifetime	—	171.0×10^6	135.0×10^6	71.0×10^4	1083	67.8×10^{25}

The first wall of the reference design consists of a water-cooled stainless steel panel. The outboard wall is an integral part of the tritium-breeding blanket and serves as the containment for the neutron multiplier. The thickness of the bare stainless steel panel is designed to allow for physical sputtering erosion and to withstand the mechanical loading projected for the full reactor life. The inboard wall is similar to the outboard wall, except that the stainless steel panel is slightly thicker to allow for vaporization erosion caused by plasma disruptions. Similar stainless steel panels are also used for the regions where preferential heat or particle fluxes occur, e.g. the limiter, beam shine-through and ripple armour regions. Where necessary, the thickness of the panel is modified to allow for enhanced erosion. All regions of the first-wall system are designed for the full reactor life under the reference operating conditions.

1.1. Operating parameters

The reference operating schedule for INTOR, based on three stages of operation, is given in Table VII-1. Stage 1 consists of a one-year hydrogen plasma operation for engineering check-out and of two years of D-T plasma operation. Stage 2 consists of four years of engineering testing and Stage 3 consists of eight years of upgraded engineering testing. The fluences and wall

TABLE VII-2. INTOR FIRST-WALL OPERATING PARAMETERS

FIRST WALL	
Total plasma chamber area	380 m^2
Average neutron wall loading	1.3 MW/m^2
Radiative power to first wall	40 MW
Charge-exchange power	4 MW
Charge-exchange current (50% D, 50% T)	1.3×10^{23} s^{-1}
Charge-exchange flux	3.3×10^{20} $m^{-2} \cdot s^{-1}$
Charge-exchange energy	200 eV
Total disruption energy	220 MJ
Disruption time	20 ms
Total average neutron flux	6.8×10^{26} n/m^2
Integrated 14-MeV neutron wall loading	6.5 $MW \cdot a/m^2$
Total number of shots	7.1×10^5
Total number of disruptions	1080
OUTBOARD WALL	
Area	266 m^2
Surface heat flux from plasma	11.6 W/cm^2
Surface heat flux from divertor	2.0 W/cm^2
Total surface heat flux	13.6 W/cm^2
Average nuclear heating	13 W/cm^3
LIMITER	
(Outboard wall at $R \approx 6$ m – top and bottom)	
Width	1 m
Area (each)	38 m^2
Total ion flux	3×10^{23} s^{-1}
Total heat flux	10 MW
Total ion heat flux	5 MW
Heat flux density	0.3 MW/m^2
Peaking factor	1.5
Typical particle energy	100 eV
Duration	4 s
Period	t = 0–4 s
RIPPLE ARMOUR	
(Outboard wall at $R \approx 6$ m – top and bottom)	
(does not coincide with the limiter)	
Area	26 m^2
Heat flux (ripple = ± 0.5%)	0.4 MW/m^2
Peaking factor	2
Particle energy (D)	120 keV
Duration	2 s
Period	t = 8–10 s

TABLE VII-2 (cont.)

INBOARD WALL	
Area	114 m^2
Surface heat flux	11.6 W/cm^2
Average nuclear heating	13 W/cm^3
Peak disruption energy density	289 J/cm^2
BEAM SHINE-THROUGH REGION	
(inboard wall)	
Total power (5% of injected)	4 MW
Particle energy	175 keV
Duration	2 s
Period	t = 4–6 s
Area	4 m^2
Heat flux	1 MW/m^2

loadings are based on 100 s shots with a 70% duty cycle in Stage 1, and on 200 s shots with an 80% duty cycle in Stages 2 and 3. The plasma burn produces a 620 MW flat-top power profile with an average neutron wall loading of 1.3 MW/m^2. The fluences listed include a peaking factor of 1.2 at the outboard regions where the test modules are located. The requirement for Stage 3 is to accumulate ~ 5 MW · a/m^2 within 8 years after the end of Stage 2. The annual neutron wall loading for Stage 3 is 0.62 MW/m^2.

The parameters specified for the INTOR first-wall system are summarized in Table VII-2.

1.2. Design description

Figure VII-1 presents a poloidal view of the reference reactor design, indicating the location of the first-wall system, i.e. outboard wall, inboard wall, limiter region, beam shine-through region and ripple armour region. All first-wall components are fabricated from Type 316 stainless steel and utilize low-pressure (< 1 MPa) water coolant. Figure VII-2 is a schematic diagram of the panel-type construction, showing the thicker flat panel that faces the plasma and the corrugated back-panel that forms the coolant channels. The two panels are diffusion-bonded together and the welded supports are spaced as required. The thickness of the plasma side-panel is sufficient to withstand the sputtering and vaporization erosion predicted for the full reactor lifetime. The present design philosophy was to avoid incorporating any separate armours for the special high-heat-flux regions, if possible, in order to keep the first-wall system design as simple

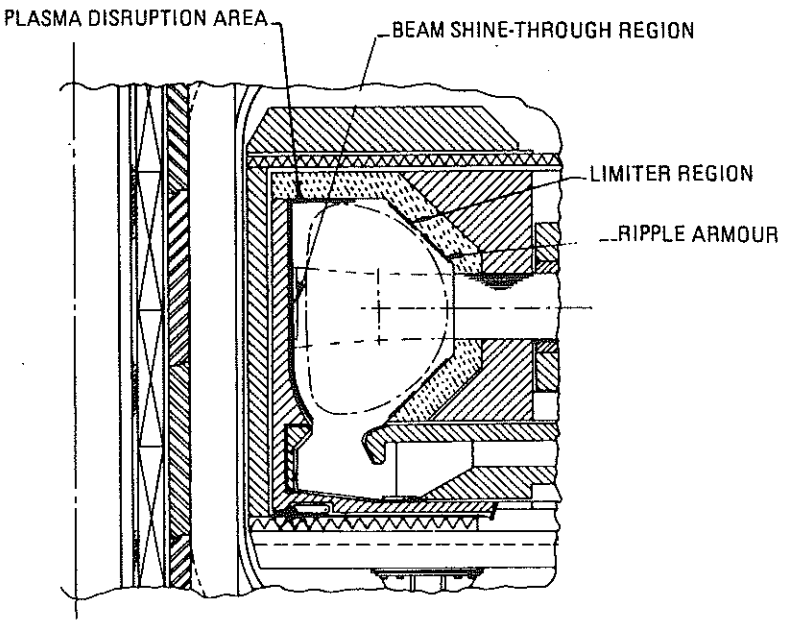

FIG. VII-1. First-wall configuration.

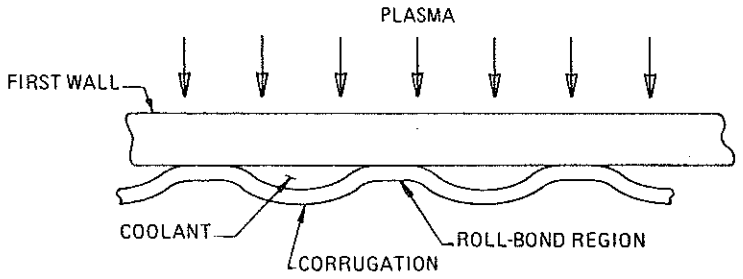

FIG. VII-2. First-wall cross-section.

as possible. As a result, the special regions, i.e. the limiter, beam shine-through and ripple armour regions, are just a part of the first wall, with minor thickness modifications to allow for effects caused by the preferential heat or particle fluxes.

The reference-design first wall is a water-cooled stainless steel panel. The low-temperature water coolant maintains the structure at temperatures commensurate with acceptable structural properties under irradiation. The low pressure also tends to minimize the primary stress requirements. The 20% cold-worked stainless steel is selected because of superior radiation damage resistance and the higher allowable design stress. The panel-type construction is proposed because of ease of fabrication, reduced stresses resulting from the thin corrugated

TABLE VII-3. SUMMARY OF THE LIFETIME ANALYSIS FOR THE FIRST-WALL REGIONS

Region	Total thickness (mm)	Maximum erosion (mm)	Maximum temperature[a] (°C)	Maximum stress[b] (MPa)	Fatigue life (cycles)	
					No erosion	With erosion[c]
Outboard wall	11.7	8.7[d]	260	360	3×10^6	$> 10^7$
Ripple region	11.7	8.7[d]	297	400	1×10^6	$> 10^7$
Limiter region	12.8	9.8[d]	280	410	8×10^5	$> 10^7$
Inboard wall	13.5	10.5[e]	275	408	9×10^5	$> 10^7$
Beam shine-through region	13.5	10.5[e]	332	495	2×10^5	$> 10^7$

[a] Maximum specified temperature = 350°C.
[b] Maximum allowable stress = 650 MPa on plasma side, 765 MPa on coolant side (cold-worked material).
[c] Assumes an erosion rate of one-half of the predicted rate for the conservative design.
[d] Physical sputtering.
[e] Physical sputtering plus vaporization.

coolant channels, and longer predicted lifetime than for tube-bank designs. The outboard wall is an integral part of the blanket and serves as the containment for the neutron multiplier. This tends to minimize structure and coolant volumes between the plasma and the breeder zone, which enhances the breeding performance. The manifolding and support structures are readily incorporated with the blanket.

The reference-design stainless steel first wall meets all design requirements and is predicted to last for the full reactor lifetime under the reference operating conditions. The design and lifetime analyses have established: (1) the allowed values for sputtering, blistering and vaporization erosion, (2) maximum temperature limits for the structure, (3) maximum stress limits for the structure, and (4) fatigue limits for the structure. Table VII-3 summarizes the results of the lifetime analysis for the various regions of the first wall.

The major uncertainties in the first-wall concept relate to the stability of the melt layer predicted to form during a disruption and the response of the beam shine-through region. The thin melt layer ($\sim 100\ \mu m$) will exist only for a short time (of the order of 10 ms). The calculated pressures induced in the melt layer are small, but additional data are required to demonstrate that the melt region does not erode. The lifetime analysis for the reference first-wall design does not

include an allowance for erosion of the melt layer. If future investigations indicate that significant portions of the melt layer erode, design modifications of the inboard wall will be required. A possible solution is a thick (30 mm) grooved-wall concept that would allow for erosion of ~ 10% of the melt layer during each disruption. It should be noted, however, that the thicknesses of the melt layer and of the vaporized region are very sensitive to the disruption conditions. Hence, any significant change in disruption conditions would most likely lead to a different design solution. A second area of major uncertainty is the beam shine-through region. A 2-s pulse exceeding ~ 1.25 to 1.5 MW/m^2 produces surface temperatures and fatigue damage in excess of the design limitations. Design modifications, e.g. a grooved wall, will also be required if higher heat fluxes are consistently deposited on this region.

1.2.1. Materials assessment

The materials data base used for the lifetime analysis of the reference first-wall design is summarized in this section (see also Section 2). Considerable experimental data on light-ion sputtering have been generated in recent years. Variations in sputtering yields have been attributed to surface roughness effects, impurity effects such as oxidation of beryllium, compositional differences in alloys, temperature effects, and unresolved differences between laboratories. Analytical expressions, such as those reported by Roth et al. [6] and Smith [7], have been developed to predict sputtering yields for materials and conditions where experimental data are not available. These analytical expressions generally agree with the reported experimental data within a factor of two, and within a factor of 1.5 in many cases. A combination of experimental data and values calculated from these analytical expressions has been used as a basis for evaluating erosion yields for the INTOR first-wall components. Table VII-4 summarizes the physical sputtering yields for stainless steel at 200 eV (the average particle energy on the first wall during a burn) and 100 eV (the particle energy on the limiter region during start-up). Note that the charge-exchange flux on the first wall is essentially all from hydrogen, with insignificant contributions from helium and other impurities.

Table VII-5 summarizes the physical sputtering erosion rates for the various regions of the stainless-steel first-wall panel. The physical sputtering erosion rates are based on effective sputtering yields of 0.017 atoms per particle at 200 eV (6.63×10^{-6} mm/s) and 0.006 atoms per particle at 100 eV (8.3×10^{-7} mm/s).

Chemical sputtering is not predicted to cause significant erosion of the stainless steel first wall under the projected operating conditions. An assessment of the blistering characteristics of stainless steel under INTOR conditions indicated that the effect of helium is not significant. However, a more detailed analysis is

TABLE VII-4. RECOMMENDED SPUTTERING YIELD VALUES FOR STAINLESS STEEL

Particle energy (eV)	Incident particle	Yield (atoms/particle)	Fraction of flux (%)	Effective yield (atoms/particle)	Fraction of yield (%)
200	D	0.011	50	0.0055	33
200	T	0.022	50	0.011	67
200	D + T	–	–	0.017[a]	100
100	D	0.004	50	0.002	33
100	T	0.008	50	0.004	67
100	D + T	–	–	0.006[b]	100

[a] Corresponds to 6.63×10^{-6} mm/s.
[b] Corresponds to 8.3×10^{-7} mm/s.

TABLE VII-5. WALL THICKNESS REQUIREMENTS FOR THE FIRST-WALL SYSTEM

	Outboard wall and ripple armour region (mm)	Inboard wall and beam shine-through region (mm)	Limiter region (mm)
Physical sputtering erosion (burn)	8.7[a]	8.7	8.7
Physical sputtering erosion (start-up)	–	–	1.1[b]
Vaporization during disruption	–	1.8[c,d]	–
Remaining wall thickness	3.0	3.0	3.0
Wall thickness required	11.7	13.5	12.8

[a] Erosion rate = 6.6×10^{-8} mm/s (2.2×10^{-8} mm/s during Stage IA).
[b] Erosion rate = 3.3×10^{-6} mm/shot (when each limiter is used during 50% of the time).
[c] Assumes that the melt layer formed during disruption does not erode.
[d] Allowance is twice the calculated value of 8×10^{-4} mm/disruption.

required to assess the importance of potential blistering caused by 3.5 MeV alpha particles.

Some uncertainty exists regarding the permeation of tritium through the first wall into the coolant. According to results from gaseous permeation studies, enhanced permeation rates may occur when energetic tritium ions are injected into the surface. A more detailed discussion of this mechanism is presented in Chapter XI.

Type 316 stainless steel in the cold-worked condition is proposed for the first-wall structure. Loss of ductility caused by displacement damage and helium generation is considered to be the most important irradiation effect for the lifetime of stainless steel. Annealed materials meet the calculated stress requirement, but cold-worked materials with their higher allowable design stress provide a significantly larger margin for safety. Cold-worked plates can readily be fabricated with the required thicknesses.

Under certain conditions, austenitic stainless steels are susceptible to intergranular cracking when exposed to pressurized water or steam at elevated temperatures. These effects are not predicted to be excessive for the relatively low-temperature ($\leqslant 100°C$) water if the water chemistry is carefully controlled. Impurities such as dissolved oxygen, chlorides and hydroxides can lead to enhanced intergranular cracking or stress corrosion cracking. Also, sensitization of the stainless steel must be avoided. The available data base indicates that the cold-worked material is more resistant to radiation damage than the annealed material. For the predicted operating conditions, swelling, embrittlement and radiation creep are not expected to be excessive.

1.2.2. Disruption effects

Three effects of plasma disruptions on the first wall were analysed in the present study, namely vaporization of the wall, formation of a melt layer, and electromagnetic loading. A comprehensive modelling effort was undertaken and analyses were performed by all participating countries to evaluate the extent of vaporization and melt-layer formation during a plasma disruption. In general, the results from the most advanced models developed by all countries are in good agreement [2 – 5]. These more rigorous models predict substantially lower vaporization rates than do the less sophisticated models. Figure VII-3 shows the calculated thicknesses of the vaporized and melted regions of stainless steel for various energy densities. The reference condition is 289 J/cm^2 during a 20 ms disruption. The thicknesses of the vaporized region are considered acceptable. However, if the melt layer were eroded during disruption, the erosion rates of stainless steel would be excessive. The surface region is molten for less than 30 ms and the regions 50 μm into the wall are molten for only a few milliseconds.

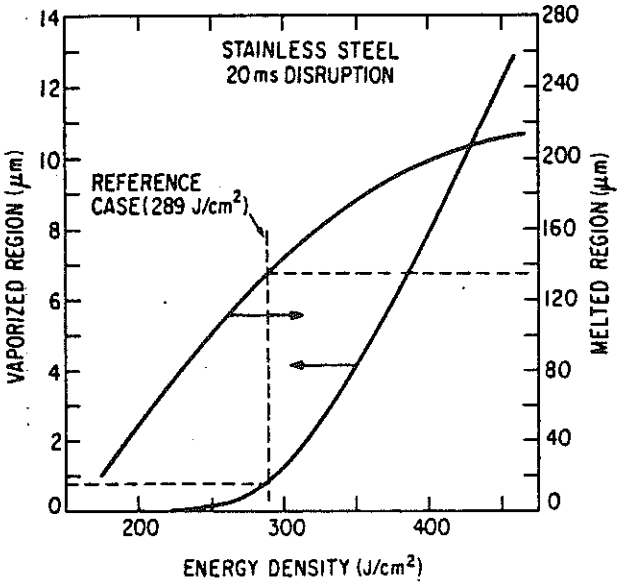

FIG. VII-3. Calculated vaporized and melted regions as a function of energy for a 20-ms disruption.

Preliminary analyses of the electromagnetic forces induced in the first wall and in the melted regions were conducted. The calculated pressures in the stainless steel melt zone are less than 275 N/m^2 (0.04 lb/in^2). The magnitude of the force reaches a maximum before melting occurs. Also, the force reverses direction and becomes compressive at ~ 12 ms for the reference disruption scenario.

1.2.3. Thermohydraulics

The thermal responses of the various regions of the first wall are summarized in Figs VII-4 to VII-6 for the specified wall thicknesses and heating rates. Figure VII-4 shows the thermal response of the 11.7-mm outboard wall and the ripple armour region for Stage-1(b) operation (100-s burn). The wall temperatures remain approximately the same for the extended burn during Stage-2 and 3 operation. The maximum temperature of ~ 260°C near the end of the burn is within the maximum temperature limit of 350°C specified. The maximum temperature would be slightly less for the actively cooled limiter. The 297°C thermal peak on the surface of the ripple armour region is also within the allowable temperature limits. Figure VII-5 shows the thermal response for the 12.8-mm-thick limiter region where the temperature near the end of the burn (280°C) is slightly higher than that of the outboard wall because of the

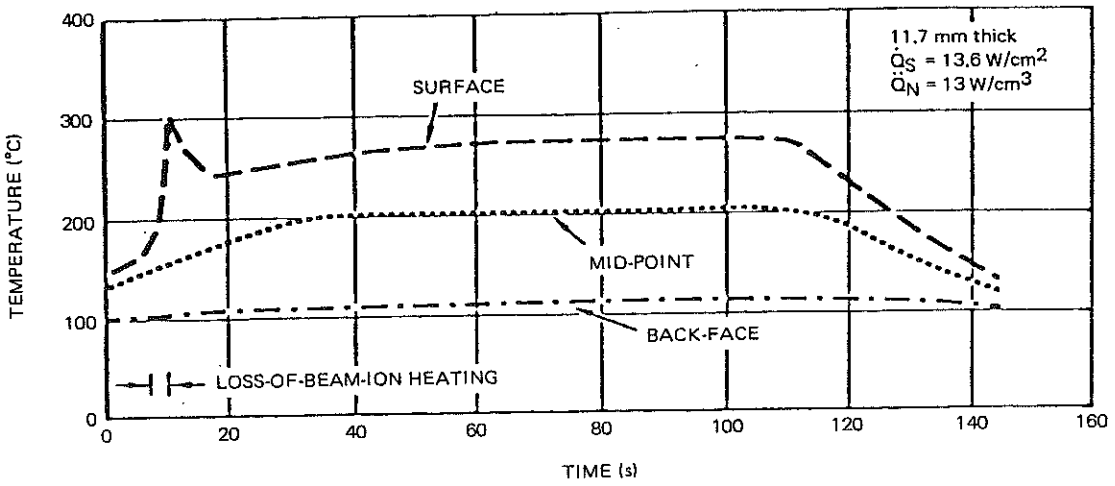

FIG. VII-4. Thermal response of outboard wall and ripple armour region.

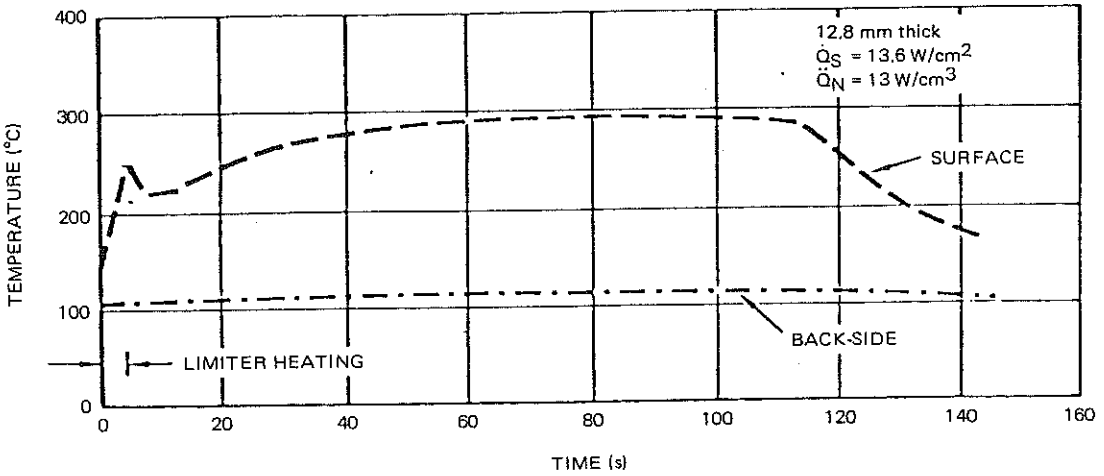

FIG. VII-5. Thermal response of limiter region.

increased wall thickness; however, the 250°C thermal peak associated with start-up is considerably less than the steady-state temperature.

The thermal response of the inboard wall is shown in Fig.VII-6. The higher steady-state temperature of the inboard wall (275°C) compared with that of the outboard wall is due primarily to the higher bulk heating in the thicker inboard wall. The neutral beam shine-through produces a 332°C thermal peak during start-up if the heat flux is 1 MW/m^2 for 2 s. A 3 MW/m^2 heat flux for the same period produces a thermal peak of ~ 700°C on the surface. Calculations indicate that no thermal peak occurs at mid-thickness of the panel.

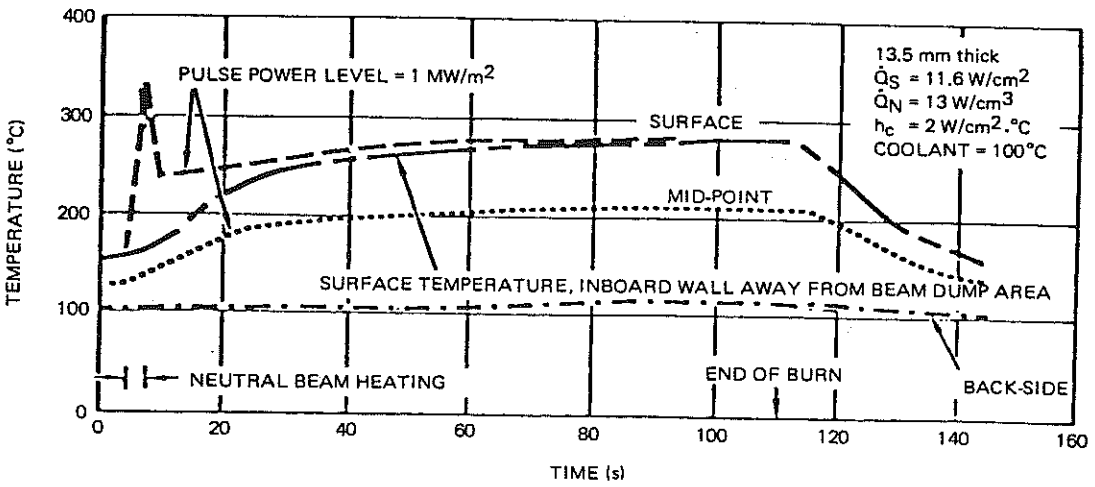

FIG. VII-6. Thermal response of inboard wall and neutral beam shine-through region.

1.2.4. Stress and lifetime analyses

Stress and lifetime analyses have been performed to guide the design of the INTOR first wall. Pressure loading, thermal loading and magnetic loading resulting from plasma disruption have been considered in the stress analysis. The analyses have taken into account the thinning of the first wall due to sputtering and vaporization. Stresses due to differential swelling have been assumed to be small in the present analysis. Lifetime analyses for a bare stainless steel wall and a grooved stainless steel wall have been performed for the reference operating parameters.

For the reference operating scenario, i.e. 7.1×10^5 cycles and 1083 disruptions over a 15-year lifetime, a solid outboard wall constructed of an 11.7-mm-thick, 20% cold-worked stainless steel panel can meet the 15 year design lifetime requirement for stress and fatigue (see Table VII-3). The maximum allowable surface heat flux corresponding to a fatigue life of 7.1×10^5 cycles is shown in Fig.VII-7 as a function of wall thickness and nuclear heating rate. The allowable heat flux (dotted lines) is greater than the expected heat flux in all cases. The cold-worked stainless steel provides a significantly larger design margin than annealed material for the maximum stress limit. Also, the design margin for fatigue life is substantially increased if advantage is taken of the reduced stresses that result from wall erosion. A conservative value of one-half of the predicted erosion rate gives a design lifetime in excess of 10^7 cycles. Similar results are derived for the 12.8-mm-thick limiter region.

If the melt layer formed during a disruption does not erode, a solid inboard wall (13.5 mm) constructed of cold-worked stainless steel will meet the full

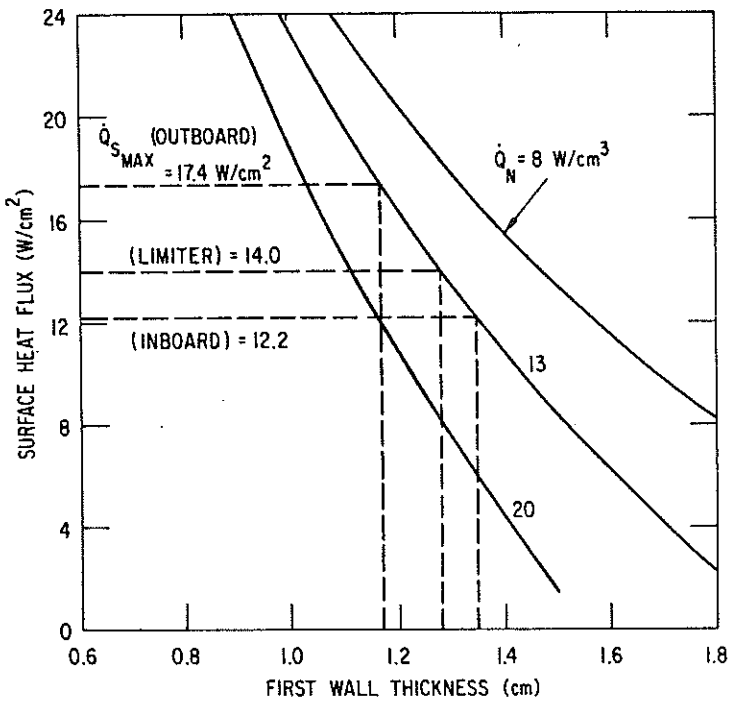

FIG. VII-7. Allowable maximum surface heat flux in a Type 316 stainless steel wall for a fatigue life of 7.1 × 10^5 cycles, as a function of wall thickness and nuclear heating rate.

15-year design lifetime. If at most 10 – 12% of the melt layer erodes during the disruptions, a grooved stainless steel inboard wall ~ 30 mm thick will last for the full 15-year design lifetime. In order to meet the full lifetime requirement for the beam shine-through region, advantage must be taken of the decreasing thermal stresses that result from thinning caused by erosion.

Coolant channels can be constructed out of thin-walled (3 – 4 mm) corrugated panels that are welded to the back of the first wall. These panels should have sufficient fatigue life, provided the water chemistry is adequately controlled, to prevent early failure due to stress corrosion or corrosion fatigue.

1.3. Back-up and alternative designs

The back-up first-wall concept consists of a radiatively cooled graphite liner on the 145 m^2 inboard wall and a water-cooled stainless-steel panel for the outboard wall. A total of 1600 graphite tiles, each 4 cm thick by 30 cm square,

are required for this design. These tiles are installed on rails and require removal of the blanket shield sector for replacement. The tiles produce 40 MW of additional nuclear heat load that must be radiated to the outboard wall and the wall behind the tiles. Tile temperatures vary from 1200°C at the start of an equilibrium burn cycle to 1300°C at the end of the cycle. The temperature of any given tile is dependent on its location and view of the cool surfaces to which it radiates.

The graphite tiles are eroded by vaporization when subjected to plasma disruptions, by chemical sputtering due to interaction with the hydrogen of the plasma, and by physical sputtering caused by high-energy plasma particle impingement. The total predicted erosion of the tiles over the lifetime of the reactor is 20 mm. Additionally, 20 mm of graphite is required at the end of the reactor lifetime to provide adequate structure in order to prevent cracking due to electromagnetic loads occurring during a plasma disruption. This results in a total thickness of 40 mm. The outboard wall is made of a water-cooled Type 316 stainless steel panel that is an integral part of the blanket assembly. Results based on more severe operating parameters indicate that a 12-mm-thick outboard wall will last for the full lifetime under the reference operating parameters.

The major concerns regarding the graphite liner concept relate to: (1) a substantial increase in the heat flux to the outboard wall caused primarily by the nuclear heating in the graphite liner; (2) design complexity and difficulties associated with the mechanical support of the tiles, and reliability of the tiles and supports under thermal stress and shock-loading conditions; (3) the large stored thermal energy in the graphite liner at the high operating temperatures (1300°C); (4) chemical sputtering and re-deposition of large amounts of graphite; and (5) radiation damage resistance of graphite. Considerable development work is required to demonstrate the viability of the graphite liner concept.

Alternative first-wall concepts considered included the use of an aluminium first-wall structure and a low-Z coating on the stainless steel first wall. A summary of the analysis for the aluminium first-wall design concept is included in the design reports [2 – 5]. It was concluded that, although the thermal stresses in an aluminium wall were lower than those for a stainless steel wall, stainless steel is preferable primarily because of the substantially larger melt layers formed and the much larger electromagnetic forces induced in the aluminium wall during a disruption. It is also concluded that the design concept using a coated (or clad) first wall provides flexibility in materials selection that could potentially eliminate the melt-layer problem associated with the stainless steel wall and the design complexity associated with the graphite liner [4]. Uncertainties regarding the reliability of the coating bond were identified as a major concern. If low-Z coatings or claddings prove to be desirable, further research and development will be required.

2. MATERIALS ASSESSMENT

The materials data base assessment conducted in the Phase-Zero INTOR study [1] provided a basis for INTOR materials selection. A more detailed materials assessment was conducted for the primary candidate materials considered in the present Phase-One INTOR design study [2 – 5]. The surface properties evaluated include physical sputtering, chemical sputtering, retention and release of hydrogen, and blistering erosion. The bulk property data base assessment focused primarily on austenitic stainless steel and graphite.

2.1. Surface properties

2.1.1. Physical sputtering

In the last few years, considerable effort has been spent on physical sputtering, including both experimental measurements and analytical and theoretical work. Important parameters considered for physical sputtering include:

- incident ion (or neutral)
- ion energy
- angle of incidence
- wall (target) material
- incident flux dependence
- incident dose dependence
- energy of sputtered species
- angular distribution of sputtered species
- wall temperature
- morphology of wall surface.

The importance of these parameters depends on the first-wall component of interest. Variations in sputtering yields have been attributed to surface roughness effects; impurity effects such as oxidation of beryllium; compositional differences in alloys; temperature effects and other unresolved differences between laboratories. Differences as large as 70% in the sputtering yields from D^+ and He^+ have been observed for as-received and polished surfaces [8]. The data on the sputtering of Be and BeO reported by Roth et al. [9] are nearly identical, indicating that the beryllium was probably oxidized by contamination. Similar results are observed for Al and Al_2O_3. Oxygen effects have also been reported for tungsten. As a result, the experimental data for materials with high oxidation potentials are subject to significant chemical effects. Stainless steel sputtering data obtained at 500°C are higher by 50% than data obtained at room temperature. This difference has been attributed by Roth et al. [10] to changes

TABLE VII-6. RECOMMENDED PHYSICAL SPUTTERING YIELDS FOR INTOR FIRST-WALL MATERIALS

Incident particle	Yield (atoms/ion)			
	Stainless steel (100 eV)	Stainless steel (200 eV)	Graphite (200 eV)	Beryllium (200 eV)
D	0.004	0.011	0.023	0.026
T	0.008	0.022	0.035	0.039
He	0.020	0.060	0.070	0.092
C	0.050	0.11	0.18	0.45
O	0.060	0.13	0.33	0.65
Fe	0.20	0.48	–	–

in the surface composition due to diffusion and preferential sputtering. Significant differences have also been reported for physical sputtering of the same material tested at different laboratories.

Analytical expressions [6, 7] have been developed to predict sputtering yields for materials and conditions where experimental data are not available. These analytical expressions generally agree with reported experimental data within a factor of 2, and within a factor of 1.5 in many cases. A combination of experimental data and values calculated from these analytical expressions have been used as a basis for evaluating erosion yields for the INTOR first-wall components (see Table VII-6). The deuterium and helium sputtering yields for stainless steel and graphite are based primarily on the data of Roth et al. [6]. The tritium sputtering yields are scaled from the deuterium values, according to the incident particle mass ratios and the analytical expression of Smith [7]. The values for physical sputtering by oxygen are based on experimental data [6] for oxygen incident on nickel, and on calculated values [7]. The calculated values for oxygen on nickel and nickel self-sputtering are in good agreement with experimental data if a binding energy value of 3.4 eV is used for nickel. Since no experimental data are available for oxygen on stainless steel, the calculated values are used. The analytical expression of Smith [7] is also used to evaluate sputtering by oxygen and carbon because the expression proposed by Roth et al. is for incident-to-target-particle mass ratios of < 0.4.

2.1.2. *Chemical sputtering*

The potential chemical erosion of first-wall materials has been evaluated for INTOR conditions [4]. The chemical effects considered include hydrogen (D-T) interactions with graphite and oxygen interactions with graphite. There is no evidence for significant chemical sputtering of stainless steel under conditions of interest. Several factors influence the magnitude of the sputtering yield or the reaction probability of graphite with hydrogen. The type of graphite employed results in yield variation of less than an order of magnitude. This variation is attributed to differences in the relative amounts of surface basal and prism planes, with prism planes exhibiting greater reactivity. Thermal atomic hydrogen attack results in lower yields than energetic hydrogen bombardment. A five-order-of-magnitude spread in yields, from 10^{-6} to 10^{-1}, has been observed. The greater reactivity under energetic bombardment may be due to increased retention of implanted as compared with adsorbed hydrogen, or to an increase in highly reactive sites due to lattice damage. A dependence of the yield on temperature has generally been observed, with a maximum in yield occurring between 720 and 920 K for methane production. The reported variation for any given study is approximately one order of magnitude. Substantial reactivity has also been observed above 1300 K. The likely product has been identified as C_2H_2, and it appears to be the prism plane that is principally responsible for the higher temperature yields. Maximum yields occur for ion energies of a few hundred eV, but the variation is less than an order of magnitude for expected ion energies. Increasing the ion flux decreases the yield and increases the temperature of the maximum yield, but a thousand-fold variation in flux results in less than a ten-fold variation in yield. Simultaneous electron bombardment can substantially increase erosion by atomic hydrogen, for which as much as a 20-fold increase has been observed at room temperature. The magnitude of the effect depends on electron energy, with observed reaction probabilities between 5×10^{-2} for 40 eV electrons and 1.6×10^{-1} for 200 eV electrons. Differences in yield have been observed for different hydrogen isotopes. A comparison of CD_4 and CH_4 production shows 50% higher production of CD_4, with the temperature maximum occurring 50 K lower.

Although considerable data have been generated on the reactions of hydrogen with graphite, there is a high degree of uncertainty in the chemical erosion rates of graphite for INTOR conditions. The data of Busharov et al. [11] have been used as a basis for predicting the chemical erosion rate (0.03 atoms/ion) of graphite at temperatures of ~ 1500 K.

In a high-temperature reactor containing graphite, any oxygen present either as atomic oxygen or in moisture (H_2O) could react with the graphite. Any moisture present would cause the following reaction:

$$H_2O + C \rightleftarrows CO + H_2$$

At high temperatures, the reaction is driven strongly to the right so that any water reaching the graphite would react to form CO. The CO would desorb and enter the plasma, resulting in chemical sputtering of the graphite. Repetitive recycling of the oxygen would lead to a C/H sputtering ratio proportional to the O/H ratio in the plasma. Atomic oxygen also exhibits substantial reactivity with graphite at high temperatures. A reaction probability of up to 0.4 has been reported [12].

2.1.3. Retention and release of hydrogen

The implications for INTOR relative to the tritium inventories in the first wall have been investigated. According to earlier calculations [13], tritium trapping in a stainless steel wall operating under INTOR conditions will not be significant. Similar calculations have been conducted for the graphite liner concept. Since graphite operates at temperatures substantially higher than those for hydrogen released from traps, the tritium inventory should not be excessive. The upper limit of the total amount of tritium retained in the graphite liner during a 3600 s discharge sequence is calculated to be between 1 g and 4 g (i.e. 10 kCi and 40 kCi), with the lower amount being much more likely [4]. Of course, when the discharge ceases, the tritium will rapidly diffuse from the liner, resulting in insignificant tritium retention levels if its solubility is low.

2.1.4. Blistering erosion

Low-energy hydrogen implantation can produce blisters on stainless steel only at low temperature and/or high flux. At a flux of 10^{15} H/cm$^2 \cdot$ s, 20 keV H^+ will produce blisters on stainless steel at 240 K, but not at 270 K [14]. Therefore, hydrogen blistering of a stainless steel wall will not occur at INTOR temperatures. Based on the critical fluence for blister formation as a function of implantation temperature, the critical concentration for hydrogen blistering is approximately 0.4 hydrogen per metal ratio. For the INTOR conditions for neutral beam shine-through (175 keV deuterons; 3 MW/m^2; 100°C wall temperature; 2 s duration), diffusion equation calculations indicate that the maximum instantaneous concentration from this neutral beam shine-through for 2 s duration is 2.5×10^{-3} deuterium per metal ratio. Thus, hydrogen blistering from this brief high-energy flux at elevated temperatures is unlikely.

Monoenergetic He^+ implantation can produce a significant surface deformation and exfoliation in metals. Maximum erosion due to repetitive flake exfoliation is observed at a temperature of ~ 0.2 to 0.3 of the absolute melting temperature [15]. There are many factors besides temperature that influence helium blistering. Of crucial importance is the incident He^+ energy spectrum. Multiple energy implantations typically reduce or eliminate blistering. Under multiple energy

TABLE VII-7. OPERATING CONDITIONS FOR THE FIRST WALL

Total 14-MeV neutron wall loading	6.5 MW·a/m^2
Bulk damage	74 displacements per atom
Gas production	
helium	980 ppm (at.)
hydrogen	3700 ppm (at.)

implantations, connected microporosity between helium bubbles is created, forming a pathway for the release of He^+ to the surface without blistering. The likelihood of blistering from 3.5 MeV alphas on unconfined orbits in an INTOR-size reactor is uncertain. Even if the conditions for blistering in a reactor were met, there are numerous modifications that can reduce the net erosion rate. Materials modifications include hardening, surface roughness and porosity. Helium blistering is, therefore, a potential source of erosion, but the deleterious consequences can be avoided by appropriate engineering design and proper choice of materials.

2.2. Bulk material properties

2.2.1. Structural material properties

The structural material for the INTOR first wall/blanket should maintain its mechanical integrity and dimensional stability under the severe radiation, thermal, chemical and stress conditions in a fusion environment. The material must be resistant to radiation damage, capable of operation at elevated temperature, compatible with other blanket materials, and capable of withstanding significant heat fluxes. In addition, there should be adequate resources for the structural material and it should be easily fabricated. Austenitic stainless steel has been found to best meet the overall requirements of a structural material and it has, therefore, been selected as the reference material. This section summarizes the relevant materials property data for both solution-annealed and 20% cold-worked Type 316 stainless steel for the INTOR operating conditions, as shown in Table VII-7.

2.2.1.1. Thermophysical properties

The thermophysical properties of Type 316 stainless steel at several temperatures are presented in Table VII-8.

TABLE VII-8. THERMOPHYSICAL PROPERTIES OF TYPE 316 STAINLESS STEEL

Property	100°C	200°C	300°C	400°C	500°C
Thermal expansion (10^{-6} K^{-1})	17.2	18.0	18.7	19.4	20.2
Thermal conductivity (W/m·K)	15.6	17.0	18.4	19.7	21.1
Heat capacity (J/kg·K)	494	524	541	553	563
Electrical resistivity (10^{-8} Ω·m)	82	88	93	98	102
Young's modulus (GPa)	189	184	176	168	159
Poisson's ratio	0.272	0.280	0.288	0.296	0.303

2.2.1.2. Tensile properties

The tensile properties of solution-annealed, 20% cold-worked, and welded Type 316 stainless steel at the upper and lower operating temperature bounds are given in Table VII-9. The tensile properties of the welded material are intermediate between those of annealed and 20% cold-worked material.

Irradiation at temperatures of < 450°C will generally increase the strength and decrease the ductility of annealed Type 316 stainless steel. The magnitude of the changes depends upon the total fluence and the irradiation temperature. There is a large data base on the effects of fast neutron irradiation at temperatures of > 370°C, but there are little data on the combined effects of high helium and displacement damage. The sparse irradiation data for temperatures of $\leqslant 350$°C are summarized in Table VII-9 [16]. The data are for a maximum damage level of 13 displacements per atom (dpa) and 740 ppm(wt)[1] He, which represent 18% and 76%, respectively, of the end-of-life levels. At 300–375°C, both the 20% cold-worked and welded forms of Type 316 stainless steel have uniform elongation of more than 1%. However, at 35°C, the uniform elongation of 20% cold-worked material is reduced to 0.4% by the modest damage levels. Weld metal maintains a uniform elongation of ~ 6% at 35°C. No data are available for annealed Type 316 stainless steel at low temperatures. Elevated temperature tests have been conducted on 20% cold-worked Type 316 stainless steel at

TABLE VII-9. TENSILE PROPERTIES OF IRRADIATED AND UNIRRADIATED AUSTENITIC STAINLESS STEEL AT TWO TEMPERATURES[a]

Material	Yield stress (MPa)		Ultimate strength (MPa)		Uniform elongation (%)		Total elongation (%)	
	T_1	T_2	T_1	T_2	T_1	T_2	T_1	T_2
20% cold-worked 316 SS								
unirradiated	810	550	850	650	5	10	13	15
irradiated	950	705	955	810	0.4	4	12	8
Solution-annealed 316 SS								
unirradiated	200	130	500	450	29	25	35	28
irradiated	–	–	–	–	–	–	–	–
18-8-2 welded SS								
unirradiated	350	238	603	443	19.5	11.5	23.1	15.0
irradiated	701	740	740	775	5.8	1.1	11.8	4.8

[a] T_1 range = 35–55°C, T_2 range = 300–375°C, fluence range = 4.5–13 displacements per atom; 100–740 ppm (at.) He.

damage levels of up to 60 dpa and helium concentrations of up to 400 ppm (at.) [1] [17]. At 450°C and 350°C the total elongation remains above 2%, up to the highest damage levels, as shown in Fig. VII-8. The uniform elongation remains above 1%. At 350°C the yield strength and ultimate strength approach 950–1000 MPa at the highest damage levels; at 450°C the yield strength drops to ~ 375 MPa and the ultimate strength drops to 525 MPa at the highest damage levels.

2.2.1.3. Fatigue

The mean fatigue curve for austenitic stainless steels at temperatures between room temperature and 427°C is shown in Fig. VII-9 [18]; the design fatigue curve is also shown beneath the mean fatigue curve. The design curve incorporates safety factors of either 2 for stress or 20 for cycles to failure, whichever is lower, in accordance with ASME specifications. The design curve has been used to test

[1] The basis on which 'parts per million' are considered is indicated after the symbol ppm, namely by weight (wt) or by atomic ratio (at.).

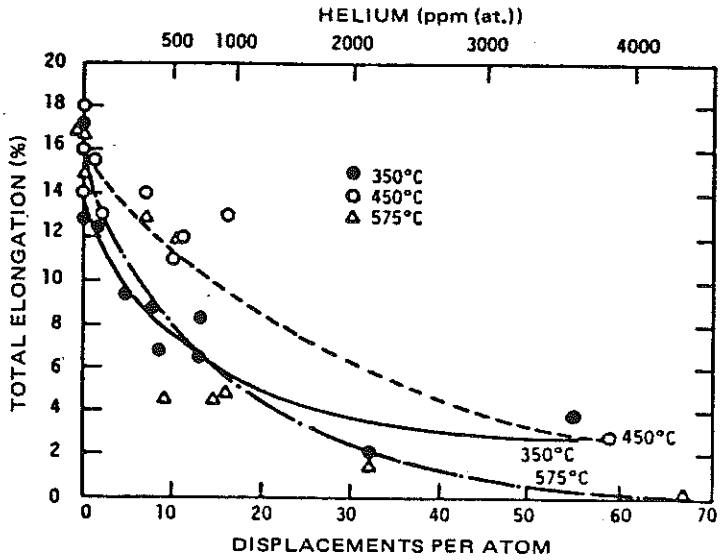

FIG. VII-8. Tensile elongation of 20% cold-worked Type 316 stainless steel irradiated in HFIR to high dpa (displacements per atom) and helium levels.

the viability of the stainless steel first-wall design. The effect of neutron irradiation on fatigue life has been investigated, and neutron radiation will, in general, reduce fatigue life in the high-strain range, but it may actually increase the lifetime in the low-strain range. Fatigue tests have been conducted on 20% cold-worked Type 316 stainless steel after irradiation in HFIR at 430°C to produce 200–1000 ppm(at.) He and 5–15 displacements per atom [19]. As shown in Fig. VII-10, unirradiated material exhibits an endurance limit at a total cyclic strain range of 0.3%. After irradiation, the low-cycle fatigue life is reduced by a factor of 3–10. However, the endurance limit is only slightly reduced to $\Delta\epsilon_t = 0.25\%$.

2.2.1.4. Swelling

Both the annealed and 20% cold-worked forms of Type 316 stainless steel are predicted to swell as a result of void formation during neutron irradiation. The swelling due to fast neutron irradiation for both materials is approximated by

$$\frac{\Delta v}{v} = R\left\{\phi t + \frac{1}{\alpha}\ln\left[\frac{1+\exp[\alpha(\tau\cdot\phi t)]}{1+\exp(\alpha\tau)}\right]\right\} \qquad (1)$$

where $\Delta v/v$ is the fractional volume change, ϕt is the neutron fluence, and R, α and τ are temperature-dependent coefficients [4]. The predicted swelling

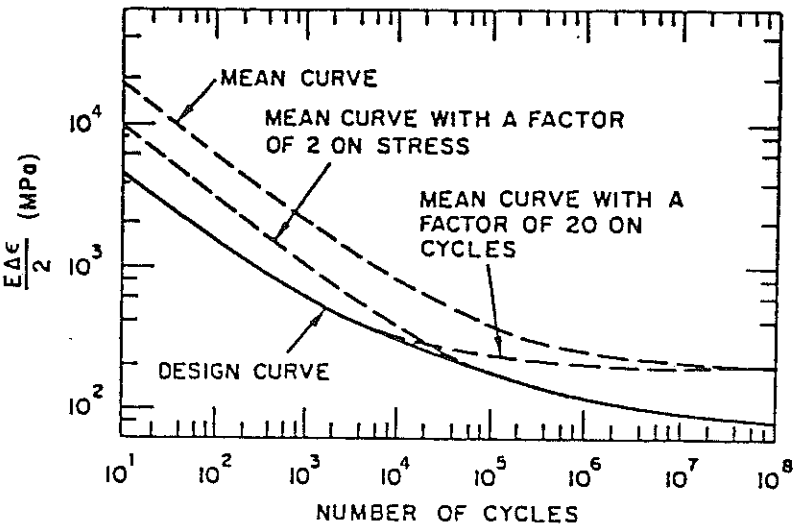

FIG. VII-9. Fatigue design curve for Type 316 stainless steel.

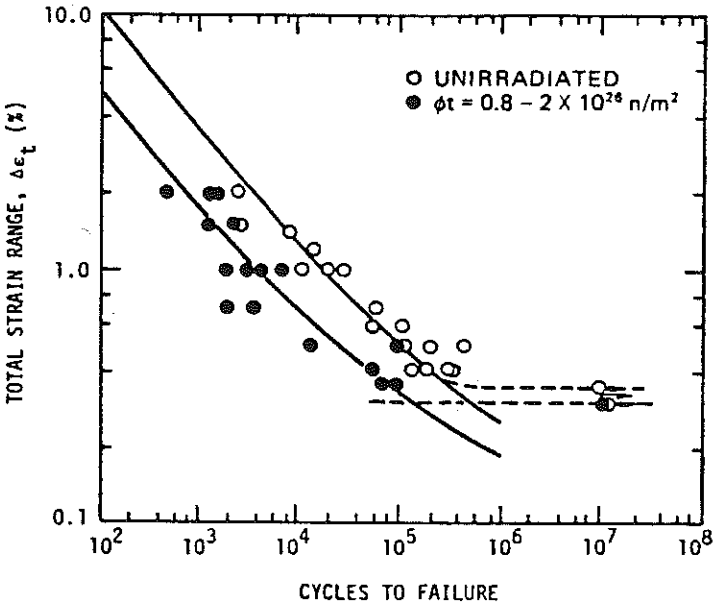

FIG. VII-10. Fatigue life of 20% cold-worked Type 316 stainless steel irradiated in HFIR at 430°C and tested at the irradiation temperature (200–1000 ppm (at.) helium, 5–15 displacements per atom).

TABLE VII-10. ESTIMATED END-OF-LIFE SWELLING OF TYPE 316 STAINLESS STEEL

Temperature (°C)	Δv/v for solution-annealed SS (%)	Δv/v for 20% cold-worked SS (%)
500	27.0	10.3
400	2.32	1.1
300	~0	~0

for both forms of Type 316 stainless steel at several temperatures for the end-of-life damage (73.5 displacements per atom) is given in Table VII-10. The high helium content produced in the first wall of INTOR is expected to influence the swelling. Recent swelling studies of 20% cold-worked Type 316 stainless steel containing a high helium concentration indicated the presence of a low-temperature swelling peak [20]. At a damage level of 7.7 displacements per atom and a helium concentration of 380 ppm (at.) the measured swelling was 0.4% at 280°C. The physical mechanisms responsible for the low-temperature swelling peak are not known, and more work is required to understand this phenomenon. No similar data are available for solution-annealed material.

2.2.2. Graphite data base

Graphite tiles have been examined as a protective armour for the inboard first wall. The property considerations for various types of graphite are reviewed in detail in Ref.[4], and only a summary is presented here. Recently, isotropic high-strain graphites have been developed which offer several attractive features. The candidate graphite from this class selected for INTOR is GraphNOL-N3M, and its physical properties are shown in Table VII-11. This graphite has a high strain capacity, excellent thermal shock resistance, and low outgassing characteristics.

The radiation behaviour of GraphNOL-N3M is not well characterized, but several general conclusions can be made from the results of irradiation studies of other graphites. The overriding consideration in determining the in-reactor lifetime of graphite is the point at which its mechanical integrity is destroyed because of internal fracture generated by radiation distortion. In general, graphite density will initially increase to a maximum value and then decrease with irradiation. The mechanical properties degrade shortly after the graphite returns

TABLE VII-11. SOME PROPERTIES OF UNIRRADIATED GraphNOL-N3M at 1100°C

	With grain	Across grain
Tensile strength	44.9 MPa	42.8 MPa
Strain to failure (tensile)	0.90%	0.95%
Thermal expansion (20°C)	0.52%/°C	0.58%/°C
Young's modulus		
tensile	8.28 GPa	7.52 GPa
compressive	10.26 GPa	8.26 GPa
Thermal conductivity	108 W/m·K	98.1 W/m·K

to its original density. Based upon this definition, the estimated lifetime value for high-strain graphites is 1.5–6 MW · a/m² [4]. The exact lifetime depends upon the irradiation temperature, with the minimum lifetime at ~ 1000°C [4]. A secondary maximum in the lifetime may occur at higher irradiation temperatures. Other properties, such as thermal conductivity and thermal expansion, will also change with irradiation. The saturation value for the thermal conductivity is estimated to be ~ 30 W/m · K, independent of temperature. The thermal expansion coefficient increases rapidly with irradiation to a maximum value of ~ 50% above the value without irradiation. It then decreases with further irradiation and reaches a saturation value of ~ 75% of the original value. Additional irradiation experiments of GraphNOL-N3M are required to determine its behaviour at end-of-life fluence levels.

2.3. Coolant compatibility

Austenitic stainless steels, in general, have good corrosion resistance to degassed high-temperature water. The corrosion resistance is attributed primarily to the formation of an adherent protective spinel film of the type M_3O_4. The corrosion rate under well-controlled conditions is about 5 mg/dm² per month or about 0.75 μm/a.

The major concerns regarding compatibility of stainless steel and water relate to effects of water purity, stress, and steel microstructure. Sensitization, i.e. precipitation of chromium carbides at grain boundaries occurring after certain heat treatments, appears to have little effect on the corrosion rate of

stainless steels in pressurized water with a pH of 7 to 11. However, intergranular attack has been observed in both Type 304 and Type 316 stainless steel exposed to water with a pH of 3.5 [21]. Stress corrosion cracking can occur on stainless steel structural components, particularly under heat transfer conditions where steam blanketing can occur or at liquid/vapour interfaces providing alternate wetting and drying. The principal problems in this area relate to boiling-water reactor or steam-generator applications where chlorides or free caustic water become sufficiently concentrated to produce cracking. If a concentrating mechanism is present, chloride and caustic concentrations of the order of parts per million in the bulk water can cause cracking. It is generally agreed that some oxygen is required to cause chloride cracking, but none is required for caustic cracking.

Hydrogen additions to water reduce the tendency for corrosion cracking. The most susceptible areas are welds and the heat-affected zones where microstructural changes have occurred and a residual stress is often present. The microstructural effects in the heat-affected zones can be minimized by either reducing the carbon content or adding stabilizers such as Ti, Nb or Ta to the stainless steel. Cold-worked materials are generally regarded as being more susceptible to stress-corrosion effects than solution-annealed materials.

Since the INTOR application is quite severe in that it includes: (1) cyclic thermal stresses, (2) radiation that can cause hydrolysis of the water and microstructural changes in the steel, and (3) cold-worked material, attention must be given to compatibility problems. However, with careful control of the water chemistry and steel microstructure, it is concluded that satisfactory performance should be attainable for the low-pressure, low-temperature conditions projected for INTOR.

3. NEUTRONICS

This section presents the neutronics analysis of the reference first-wall system design. The reference system includes: (1) a 1.5-cm-thick inboard stainless steel (SS) armour; (2) a 1.34-cm-thick outboard SS armour; and (3) a 0.6-cm-thick inboard/outboard first wall, represented neutronically by 45.5% SS + 54.5% heavy water coolant (D_2O). The outboard first wall is followed by a 5-cm-thick lead neutron multiplier and a 0.45-cm-thick (66.7% SS + 33.3% D_2O) second wall which separates the first-wall system from the tritium-breeding blanket. A comparative analysis of several candidate armour/first-wall designs studied in the Phase-One INTOR design has been given in Refs [2–5]. This section focuses on the nuclear characteristics of the reference first-wall design, based on a multi-dimensional Monte Carlo transport calculation using the MORSE code [22]. The number of 14 MeV source neutron histories generated

TABLE VII-12. POLOIDAL VARIATION OF NEUTRON AND PHOTON FLUXES AT SEVERAL SS ARMOUR REGIONS

Location	Flux $(n/m^2 \cdot s) \times 10^{-18}$ [a]				
	Neutrons				Photons
	$E \geqslant 0$	$E \geqslant 0.1$ MeV	$E \geqslant 1$ MeV	$E \geqslant 10$ MeV	$E \geqslant 0$
Inboard	5.03 (± 1%)[b]	2.93 (± 2%)	1.53 (± 3%)	0.75 (± 3%)	2.05 (± 3%)
Inner upper corner	5.14 (± 3%)	3.21 (± 4%)	1.66 (± 5%)	0.67 (± 6%)	1.70 (± 8%)
Top	5.30 (± 2%)	3.18 (± 3%)	1.67 (± 4%)	0.75 (± 4%)	1.72 (± 5%)
Outer upper corner	5.63 (± 2%)	3.51 (± 2%)	1.90 (± 3%)	0.89 (± 3%)	1.94 (± 4%)
Outboard	5.31 (± 2%)	3.34 (± 2%)	1.85 (± 2%)	0.91 (± 2%)	1.82 (± 3%)
Outer lower corner	5.57 (± 2%)	3.50 (± 2%)	1.93 (± 3%)	0.92 (± 3%)	1.93 (± 3%)

[a] Based on a neutron wall loading of 1.3 MW/m^2.
[b] Statistical standard deviation as estimated by MORSE with 20 000 neutron histories.

is 20 000; the associated data libraries [23, 24] for the transport and response rate calculations are based on ENDF/B-IV.

Table VII-12 shows the poloidal variation of neutron and photon fluxes in the SS armour. The fluxes are shifted toward the outboard direction because of MHD plasma shifting and the toroidal curvature effect [25]. The neutron flux shifting is most significant at high energies, resulting in an ~ 40% difference between the maximum and minimum fluxes for $E \geqslant 10$ MeV. On the other hand, the photon flux is higher in the inboard armour because of the high (n,γ) reaction rate present in the non-breeding inboard blanket. Except for the inboard photon flux, the total particle fluxes ($E \geqslant 0$) shown in Table VII-12, depending upon the poloidal locations, are ~ 15–30% lower than the nominal (1-D calculations with average neutron wall load) neutron and photon fluxes of 7.04×10^{18} $n/m^2 \cdot s$ and 1.96×10^{18} $n/m^2 \cdot s$, respectively. The results given in Table VII-12 are for fluxes averaged over zones of the first wall (inboard, outboard, etc.). Since the first wall does not uniformly circumscribe the plasma, significant variations in the flux occur within each zone.

TABLE VII-13. RADIATION RESPONSE RATES AT SEVERAL POLOIDAL LOCATIONS IN THE SS ARMOUR

Location	Nuclear heating (MW/m^2)[a]	Hydrogen production (ppm (at.))[b]	Helium production (ppm (at.))[b]	Atomic displacement (ppm (at.))[b]
Inboard	12.9 (± 3%)[d]	376 (± 3%)	103 (± 3%)	8.4 (± 2%)
Inner upper corner	10.8 (± 8%)	322 (± 6%)	88 (± 7%)	7.8 (± 5%)
Top	11.7 (± 5%)	355 (± 4%)	97 (± 4%)	8.5 (± 3%)
Outer upper corner	13.7 (± 3%)	481 (± 3%)	132 (± 3%)	10.6 (± 2%)
Outboard	13.1 (± 3%)	474 (± 2%)	131 (± 2%)	10.4 (± 2%)
Outer lower corner	13.0 (± 3%)	449 (± 3%)	122 (± 3%)	10.2 (± 2%)
Nominal response[c]	13.4	492	135	11.2

[a] Based on an average neutron wall loading of 1.3 MW/m^2.
[b] Based on an integral wall loading of 1.3 $MW \cdot a/m^2$.
[c] Based on a one-dimensional cylindrical model.
[d] Statistical standard deviation as estimated by MORSE with 20 000 neutron histories.

Table VII-13 summarizes the major radiation response rates averaged over each zone of the SS armour. Also included in the table are the nominal response rates based on a one-dimensional analysis. Again, the maximum response rates are found mostly in the outboard armour region. The use of heavy water as a coolant in the first and second walls results in an increase in the neutron flux and a decrease in the photon flux, relative to a light-water coolant case. For example, the nominal neutron and photon fluxes ($E \geqslant 0$) for the H_2O coolant case are estimated to be $\sim 6.32 \times 10^{18}$ $n/m^2 \cdot s$ and $\sim 2.11 \times 10^{18}$ $n/m^2 \cdot s$, respectively. These differences are caused by the less effective neutron energy moderation in D_2O, followed by a lower neutron absorption in the SS armour and hence by a reduced photon generation. Such a difference is reflected primarily in the nuclear heating rate in the armour. The nominal heating rate of 13.4 MW/m^3 shown in Table VII-13, for instance, is compared with 14.6 MW/m^3 for the H_2O coolant case. The effect of coolant selection upon the radiation damage to the

TABLE VII-14. NORMAL PLASMA OPERATING THERMAL LOAD

Surface heat fluxes		
Radiative	10.5 W/cm^2	
C-X neutrals	1.1 W/cm^2	
Charged particles	0	
Total	11.6 W/cm^2	(from plasma)
Bulk nuclear heating (spatial average at P_N = 1.3 MW/m^3)		
Stainless steel	13.0 W/cm^3	
Graphite	7.5 W/cm^3	

armour, such as gas production and atomic displacement, is of less significance since the damage is induced mostly by high-energy neutrons.

The total energy deposition of the reference INTOR design is ~ 17.06 MeV per source neutron, approximately 28% of the energy (~ 4.8 MeV) being deposited in the first-wall system including the lead multiplier and the second wall.

4. THERMOHYDRAULIC ANALYSES

The purpose of these thermohydraulic studies was to define the performance of the reference-design first wall, together with the back-up design, according to the specified thermal load conditions. These heating conditions are based on 40 MW of plasma radiative power load to the first wall. With a bare stainless steel wall as the reference-design concept, the emphasis is on examining operation under normal plasma heat loads. Table VII-14 summarizes the heat loads based on 40 MW of radiated power. Nuclear heating in stainless steel walls was assumed to be 13 W/cm^3, as indicated in Section 3.

4.1. Thermal analysis of stainless steel panels

The temperatures and associated gradients through stainless steel panels were required in order to assess material performance for the reference design. In particular, the transient responses of several first-wall areas were examined in order to provide thermal stress input data for lifetime assessments. In addition to the normal plasma heating, as given in Table VII-14, radiant flux from the hot inner divertor surface is also present. Therefore, an assessment was made to determine how much of the radiant heat flux off the front face of the divertor

TABLE VII-15. TRANSIENT HEATING DURING PLASMA START-UP

	Duration (s)	Duration of cycle (s)	Heat flux (MW/m^2)
Neutral beam shine-through	2	4–6	1[a]
Beam ripple effect	2	8–10	0.8[b]
Limiter	4	0–4	0.4[c]

[a] 5% of beam power.
[b] Includes a peaking factor of 2.
[c] Includes a peaking factor of 1.5.

is incident on the outer first-wall surfaces. This flux will be in addition to the 11.6 W/cm^2 heat load from the plasma itself.

The heat-sink divertor design results in as much as 60% of the incident power being radiated from the front face. Geometric view factors (shape factors) were computed to determine the fraction of energy leaving the divertor surface that is incident on each of the three outboard wall "facets". Details of this analysis are given in Ref.[4]. An additional radiant flux of 2.0 W/cm^2 from the divertor to the outboard wall was assumed here. This produced a total outboard wall flux of 13.6 W/cm^2.

Three specific transient heating conditions occur during the 10-s start-up period of each INTOR plasma burn. Each of these transient heating conditions has been incorporated in the present thermal analysis in order to determine the effect upon wall stresses and lifetime estimates. Table VII-15 presents a summary of the pertinent thermal data.

Neutral beam heating of the inboard wall occurs as a result of plasma penetration by the energetic neutral beam. A fraction of this injected power is not absorbed by the plasma and strikes the 13.5-mm-thick inboard wall surface. Using the thermal properties of stainless steel listed in Table VII-16, the transient response of the panel was computed with a finite-difference thermal analyser code. The results for the reference heating pulse of 1 MW/m^2 are given in Fig. VII-6. Pulse power levels of less than 2 MW/m^2 are required to maintain the maximum surface temperature of less than 500°C.

Heating of a portion of the outboard wall occurs during start-up as a result of ripple effects at the end of neutral beam injection. The heating occurs on a

TABLE VII-16. THERMAL PROPERTIES OF STAINLESS STEEL AND GRAPHITE

	Stainless steel	Graphite
Thermal conductivity (W/m·K)	18	30
Density (kg/m^3)	7900	1880
Specific heat (J/kg·K)	510	1750

toroidal strip above or below the equatorial plane and is a function of plasma edge ripple. Transient heating inputs for this case were assembled using the data for 0.5% edge ripple and a peaking factor of 2 during the two-second pulse. This produced peak heating rates of 0.8 MW/m^2. During the normal plasma-burn portion of the cycle, a surface heating value of 13.6 W/cm^2 was employed. As explained above, this is comprised of 11.6 W/cm^2 from the plasma and 2.0 W/cm^2 from the hot surface of the inner divertor collector. The wall thickness in this region has been assumed to be 11.7 mm -- the reference thickness. Figure VII-4 shows the temperature response of this 11.7-mm-thick outboard wall region and indicates a peak surface temperature (297°C) that is only slightly higher than the steady-state surface temperature (260°C).

The third transient heating pulse also occurs on a portion of the outboard wall during start-up as the plasma forms and results from the wall acting as a "limiter" to define the plasma edge. Possibly, this limiter heating occurs at the same location as ripple ion heating, but for the present study this was not assumed to be the case. In addition, the wall thickness in this region has been increased from 11.7 mm to 12.8 mm because of additional sputtering that occurs during this start-up period. The heat flux during the four-second heating pulse is 0.4 MW/m^2, including a peaking factor of 1.5. Surface heating during the normal plasma burn was again assumed to be 13.6 W/cm^2. Figure VII-5 shows the thermal response to these heating conditions. The results indicate that limiter heating produces a peak surface temperature of 250°C, which is less than the steady-state value of 280°C.

In summary, the thermal response of first walls to the three transient heating conditions indicates that neutral beam shine-through is the most severe heating condition. Limiter heating appears to be the least troublesome. In all cases, the steady-state maximum surface temperature falls below the specified maximum allowable structural temperature of 350°C.

4.2. Thermal analysis of the stainless steel tube wall

Fabrication of the stainless steel wall from tubes rather than flat panels has been suggested for INTOR first walls. Previous studies [2 – 5] have included detailed two-dimensional thermal analyses of such tube design and the present results have been derived from these earlier studies. The tube geometry results in higher ΔT_{wall} values for tubes than for flat panels under equivalent heating conditions. In fact, the results indicate that a 2-cm-ID tube with a 1-cm-thick wall would produce a value of $\Delta T_{tube} \approx 1.25\ \Delta T_{wall}$, where ΔT_{wall} can be taken from Fig. VII-4. Therefore, for the 40 MW heating case, an outboard stainless steel tube would have a maximum temperature of 300°C, compared with 260°C for a panel.

4.3. Thermal analysis of the inboard graphite armour

The use of a radiatively cooled graphite liner on the inboard wall was investigated in some detail before arriving at the present bare stainless steel wall design concept. The graphite liner was proposed to protect the inboard wall from excessive erosion caused by plasma disruptions. However, since the passively cooled armour of this back-up design largely defines the outboard wall heating conditions, the thermal study focused initially on the response of the armour to normal plasma operating heat loads. Table VII-14 summarizes the thermal input data for the study. The 10.5 W/cm^2 load corresponds to the assumed 40 MW total radiative load. Average nuclear heating values were used in these studies, keeping in mind that further refinement of the analysis will include the spatial distribution of nuclear heating, which becomes increasingly important at large thicknesses. The thermal properties of graphite are functions of operating temperature and irradiation levels. For the purposes of this analysis, the properties given in Table VII-16 were employed. Temperature responses were obtained from a finite-difference code which was used to model the specific reactor geometry of INTOR.

Figure VII-11 presents results of an analysis for the 50-mm-thick reference design armour on the inboard wall, with an average geometric view factor of 0.7 to the cooler outboard surfaces. The 70% duty cycle (100 s plasma burn, 40 s dwell plus shut-down and start-up) produces maximum armour surface temperatures of 1320°C under these conditions, and a minimum of 1215°C at the end of the dwell period. It should be noted that these values are for an equilibrium cycle variation, after approximately ten operating cycles if the system is initially started from room temperature. The effects of graphite surface temperatures, which are in the methane generation range of 400 – 800°C during this ten-cycle start-up period, have not been assessed in this study. The corresponding gradients shown in Fig. VII-11 were used to define internal thermal stresses, as described in

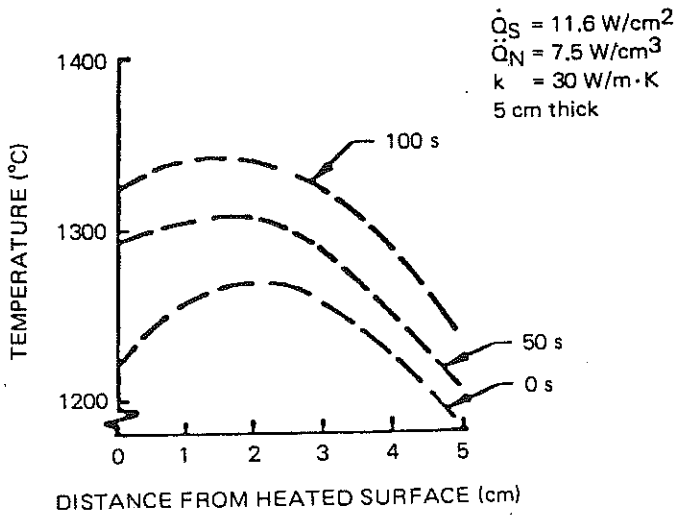

FIG. VII-11. Internal temperature distribution in the inboard graphite armour.

Section 5.2. The maximum armour surface temperature is approximately 70°C hotter on the top location, primarily because of a lower average view factor (0.5) to the outboard wall. With inboard and top armour surface temperatures defined, the radiant heat flux from these surfaces to the outboard wall surfaces was calculated. It was shown that the radiating armour adds about 18 W/cm^2 to the already existing radiant heat load from the plasma. The total surface heat load at the outboard wall is seen to be slightly over 30 W/cm^2, and this value will be used to define outboard wall operating temperatures. Parametric analyses of the graphite armour were performed to determine its sensitivity to conductivity, armour thickness, heat flux, and geometric view factor [4].

One method of attaching the graphite armour to the inboard wall is shown schematically in Section 8. An initial thermal analysis was made to define the local temperatures of the armour and water-cooled support rail for this concept. Because of uncertainties regarding the thermal contact between the rail and armour, three "bracketing" assumptions were made:

(a) Radiation only between armour and rail surfaces
(b) Intimate contact between armour and rail surfaces
(c) Radiation between all armour/rail surfaces, except for the most inboard armour/rail surfaces, which are assumed to be in intimate contact.

Temperatures were obtained for each assumption, for steady-state conditions, at a surface heat flux of 11.6 W/cm^2 and an average nuclear heating of 7.5 W/cm^3. These results indicate that loose mounting of the armour to the rails is desirable in order to minimize thermal gradients in the graphite near the mounting rail. These temperature distributions were used to compute thermally induced stresses, as described in Section 5.2.

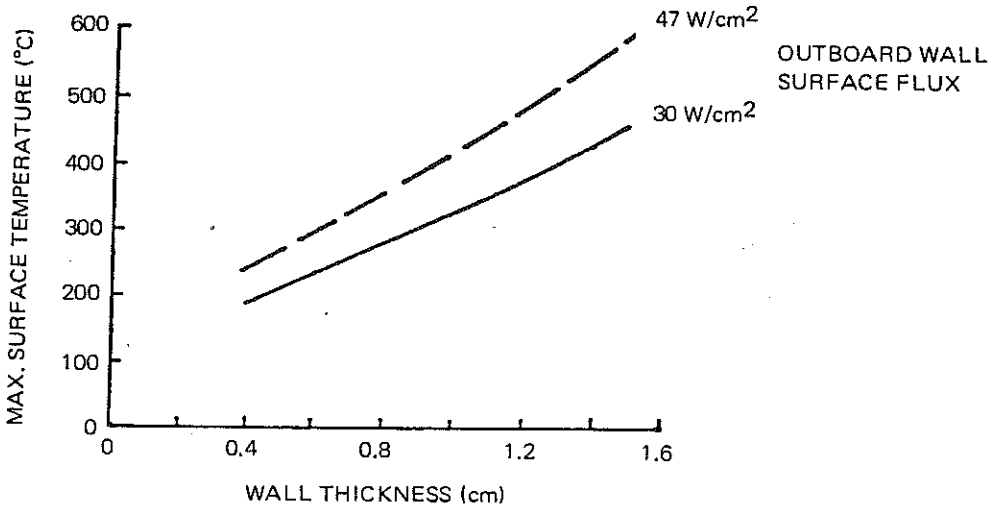

FIG. VII-12. Maximum temperature of the outboard wall with inboard graphite armour.

4.4. Thermal analysis of stainless steel panel with inboard graphite armour

The temperatures and associated gradients through stainless steel outboard wall panels were required in order to assess material performance for this back-up design option. The purpose of this analysis was to supply preliminary results so that strength and fatigue estimates could be made. The approach taken here was to compute the steady-state thermal gradient that would exist through a given thickness of stainless steel subjected to the surface heat fluxes described in Section 4.3 and to volumetric nuclear heating.

The results for the outboard wall of the back-up design are shown in Figs VII-12 and VII-13. Depending upon the plasma radiation load (40 MW or 80 MW), the outboard surface flux is 30 W/cm^2 or 47 W/cm^2, and these loads produce maximum stainless steel temperatures of 330 and 420°C, respectively, for a 10 mm wall thickness. The temperature distributions through this thickness are very nearly linear under these heating conditions.

The graphite surface temperature drops by only 115°C between successive burn cycles and, therefore, significant heat is thermally radiated to the bare stainless steel outboard wall during this time. This heat flux maintains a thermal gradient in the steel wall between the cycles. Analyses have shown that the temperature difference across the outboard wall thickness drops to 40% of the end-of-burn value between successive burn cycles. The result is a reduction in the cyclic thermal stresses in the outboard wall compared with the case where the gradient goes to zero between burn cycles.

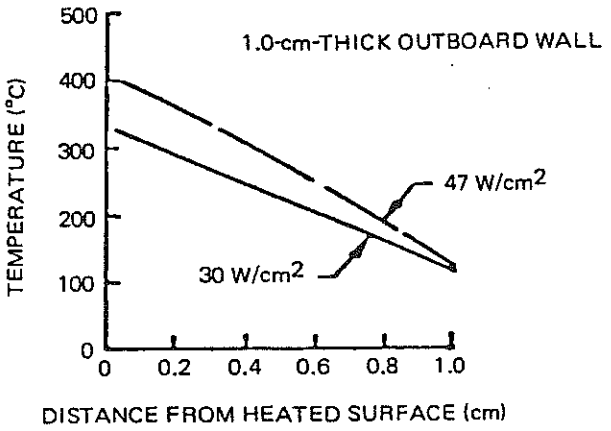

FIG. VII-13. Temperature distribution in the outboard wall (1 cm thick) with inboard graphite armour.

5. STRESS ANALYSIS

5.1. Cyclic stress and lifetime analysis of stainless steel first wall

The three-stage INTOR operating scenario for which the first-wall performance was evaluated is given in Section 1.1. The scenario results in a total of 7.1×10^5 cycles and 1083 disruptions over a 15-year reactor lifetime. Pressure loading, thermal loading and magnetic loading resulting from plasma disruption have been considered in the stress analysis. Lifetime analyses of the first wall have been performed for a solid stainless steel wall as well as for a grooved stainless steel design for the inboard wall.

If the melt layer created on the inboard wall during disruptions stays in place, a solid inboard wall (1.35 cm) made of 20% cold-worked Type 316 stainless steel can meet the full 15-year design lifetime requirement without replacement. If no more than 7% of the melt layer is removed during disruptions, a grooved Type 316 stainless steel inboard wall (2.46 cm) will be required. If disruptions do not land on the outboard wall, a solid 20% cold-worked stainless steel wall (1.17 cm) can meet the 15-year lifetime requirement without replacement. A similar conclusion can be drawn for the limiter regions (1.28 cm) of the outboard wall.

Coolant channels can be constructed out of thin-walled (3 – 4 mm) corrugated panels that are welded to the back of the first wall. These panels should have sufficient fatigue life, provided the coolant chemistry is adequately controlled to prevent early failure due to stress corrosion or corrosion fatigue.

5.1.1. Stress analysis

The assumptions underlying the stress analysis and the details of stress analysis methods used in the present report have been published previously [3,4]. Most of the stress calculations presented in this section were based on 2-D models. The results from the limited 3-D calculations indicate that slightly higher stresses may occur in some regions because of external constraints.

5.1.2. Allowable stresses

According to the procedure in the ASME Boiler and Pressure Vessel Code, Section III, the primary allowable stress, S_m, is determined from the minimum of the following four stress intensities:

1/3 S_u (ultimate strength) at room temperature
1/3 S_u at operating temperature
2/3 S_y (yield strength) at room temperature
0.9 S_y at operating temperature

Figure VII-14 shows the S_m values for both annealed and 20% cold-worked Type 316 stainless steel. Note that the ultimate strength controls the allowable stress for the 20% cold-worked material and the yield strength controls the allowable stress for the annealed material. Strain cycles as well as radiation will significantly increase the yield strength of the annealed material, thereby increasing the S_m values.

The primary stresses in the INTOR first wall due to coolant pressure and electromagnetic forces during disruption are small. The major stress in the first wall is thermal which, being a secondary stress, has an allowable value of 3 S_m. When peak stresses such as those at the root of a notch are included, the allowable stress depends on the fatigue properties of the material. Figure VII-9 shows the mean fatigue curve for a variety of austenitic stainless steels at temperatures ranging between 21 and 427°C. The ordinate in the plot is not the stress amplitude but the principal strain amplitude, multiplied by Young's modulus (1.9×10^5 MPa). Following the procedure in the ASME Code Case N47, safety factors of 2 on stress and 20 on life are applied on the mean curve to obtain the design curve. The effects of radiation on the shape of the fatigue curve have been assumed to be small.

5.1.3. Notch fatigue

On the basis of earlier reports [3, 4], the effective stress concentration factor (K_F) for the grooved configuration has been taken to be equal to 2.

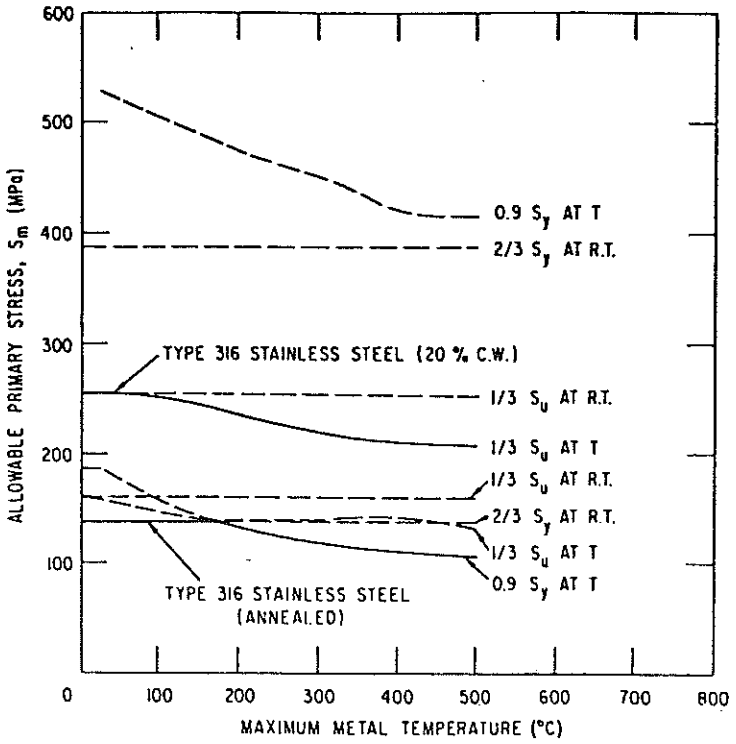

FIG. VII-14. Allowable primary stress for annealed and 20% cold-worked Type 316 stainless steel.

5.1.4. Results

Table VII-17 gives a summary of the maximum stresses due to thermal and electromagnetic forces during disruptions. The stresses due to electromagnetic forces are small compared with the thermal stresses. Note that the maximum stresses in the outboard and inboard walls during steady-state burn are within the allowable values for both the 20% cold-worked and annealed forms of Type 316 stainless steel. However, the annealed material is probably not strong enough to allow for additional stresses due to external constraints on the first wall. The maximum stresses during transients such as neutral beam shine-through (1 MW/m^2) on the inboard wall and heating due to plasma ripple effects on the outboard wall are well within the allowable values for the 20% cold-worked material, but they are insignificantly above the allowable values for the annealed material. However, being highly localized in nature, they may be treated as peak stresses and exempted from the 3 S_m requirements.

Figure VII-7 shows the maximum allowable surface heat flux corresponding to a fatigue life of 7.1×10^5 cycles, as a function of the first-wall thickness and

TABLE VII-17. ALLOWABLE AND CALCULATED MAXIMUM STRESSES AT VARIOUS REGIONS OF THE FIRST WALL (SOLID) BASED ON INITIAL THICKNESS

Region	Plasma side				Coolant side			
			Allowable stresses				Allowable stresses	
	Temp. (°C)	Stress[a] (MPa)	20% CW SS (MPa)	Annealed SS (MPa)	Temp. (°C)	Stress[a] (MPa)	20% CW SS (MPa)	Annealed SS (MPa)
Inboard wall	275	−313	−672	−364	114	415	745	414
Beam shine-through (1 MW/m^2)	332	−502	−651	−352	104	196	755	414
Outboard wall	260	−294	−670	−372	114	371	745	414
Ripple	297	−410	−662	−352	104	188	755	414
Limiter	280	−326	−666	−362	114	418	745	414

[a] Stress due to thermal and electromagnetic forces. Positive and negative signs denote tensile and compressive stresses, respectively.

the nuclear heating rate, for fatigue cycles between zero heat load and steady-state burn. The maximum allowable surface heat flux (dotted lines) is greater than the expected surface heat flux in all cases. Table VII-18 gives a summary of the lifetime analysis. The fatigue lives have been computed both on the basis of initial wall thickness and by taking advantage of the stress reduction due to wall thinning caused by erosion and evaporation during disruptions. Note that, except for the neutral beam shine-through on the inboard wall, the walls have adequate lifetimes in all cases, even if no advantage is taken of the beneficial stress effect due to erosion. Such effects would have to be considered in order to meet the fatigue life requirement if the external constraints on the first wall cause significant stresses. The effect of the neutral beam shine-through (1 MW/m^2) on the inboard wall is to limit the allowable fatigue life to 2×10^5 cycles on the plasma side of the wall. However, since more than 3 mm of the inboard wall, on the average, will be eroded away from the plasma side in 2×10^5 cycles, it is likely that any crack initiated during this time will also be removed.

The assumption so far has been that the melt layer on the inboard wall remains in place during disruptions. If a portion of the melt layer is removed during disruptions, a grooved inboard wall of an initial thickness of 2.46 cm will be required for a surface heat flux of 11.6 W/cm^2 and a nuclear heating rate of 13 W/cm^3, as shown in Fig. VII-15. Such a wall can sustain the removal of no more than 7% of the melt layer by disruptions and still meet the 7.1×10^5 cyclic life requirement. Optimization of parameters such as the depth and spacing of the grooves will have to be based on a more detailed (possibly 3-D) stress analysis of the grooved geometry. A preliminary stress analysis (2-D) of the grooved geometry has been reported in Refs [3, 4].

The integrity of the corrugated coolant channels welded to the back of the first wall has been conservatively analysed by treating the junction of the two as a series of co-linear cracks separated by ligaments represented by the regions of bonding between the corrugated panel and the first wall. Figure VII-16 shows the stress intensity factors for both thermal and coolant pressure loading (0.7 MPa) as functions of the corrugated wall thickness and the length of the bonded region in the outboard wall. The thermal component of the stress intensity factor is by far the greater of the two. By restricting the corrugated panel to a thickness of 3 mm and providing a minimum bond length of 3.5 mm, the thermal component can be kept below 4.6 MPa · m so that the crack growth is negligible. However, care must be taken in controlling the coolant chemistry so that cracks do not grow by stress corrosion or corrosion fatigue.

A lifetime analysis based on earlier operating parameters (1.1×10^6 shots and a surface heat flux of 31 W/cm^2) was performed for a stainless steel outboard wall of the back-up design which incorporates a radiatively cooled graphite liner on the inboard wall [4]. A cold-worked stainless steel wall, 1.2 cm thick, will meet the stress requirements and provide adequate fatigue life if advantage is taken

TABLE VII-18. SUMMARY OF LIFETIME ANALYSIS

Region	Total thickness (mm)	Maximum erosion (mm)	Maximum temperature[a] (°C)	Maximum strain range (%)	Fatigue life[b]	
					No erosion	With erosion[c]
Inboard wall	13.5	10.5[d]	275	0.150	9×10^5	$> 10^7$
Beam shine-through ($1\ MW/m^2$)	13.5	10.5[d]	332	0.182	2×10^5	$> 10^7$
Outboard wall	11.7	8.7[e]	260	0.133	3×10^6	$> 10^7$
Ripple	11.7	8.7[e]	297	0.147	1×10^6	$> 10^7$
Limiter	12.8	9.8[e]	280	0.151	8×10^5	$> 10^7$

[a] Maximum specified temperature = 360°C.

[b] Fatigue life computed by $N_f = \left(\frac{62613}{1.9 \times 10^5 \Delta\epsilon - 218} \right)^2$

[c] Assumes an erosion rate of one-half of the predicted rate for a conservative design.

[d] Physical sputtering plus vaporization.

[d] Physical sputtering.

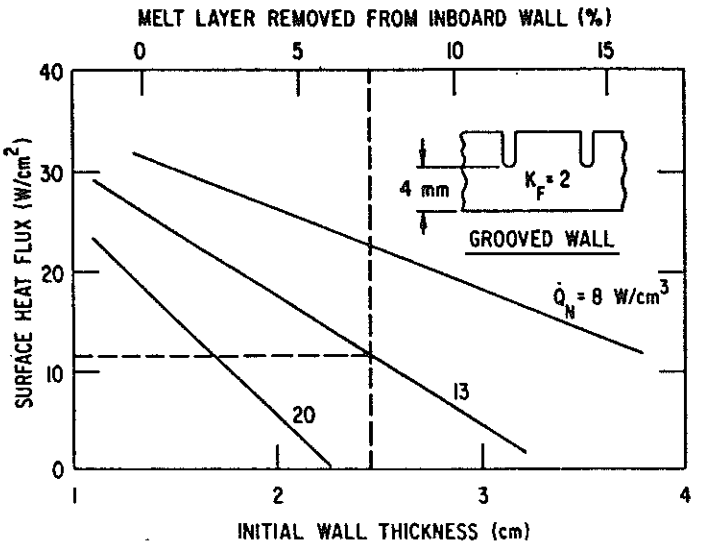

FIG. VII-15. Allowable surface heat flux for a fatigue life of 7.1 X 10^5 cycles in a grooved inboard wall of Type 316 stainless steel as a function of wall thickness, nuclear heating rate and percentage of melt layer removed.

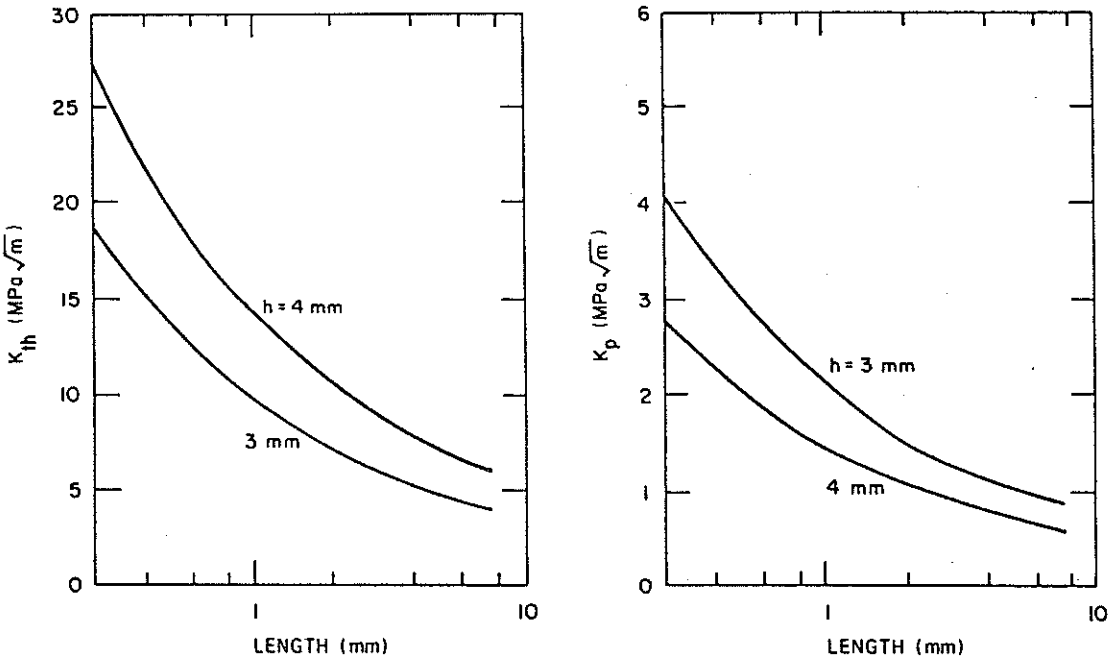

FIG. VII-16. Stress intensity factors due to thermal loading (K_{th}) and coolant pressure loading (K_p) as functions of the length of the bonded region between the corrugated panel and the first wall.

of the reduction in the cyclic stress that results from wall thinning during operation. The present reference operating parameters, i.e. 7.1×10^5 shots and 1083 disruptions, are considerably less severe than those analysed. Therefore, the surface heat flux to the outboard wall will be less, since the thickness of the graphite liner, and hence the radiative heat load, can be reduced. On this basis, a full reactor lifetime is predicted for a 1.2-cm-thick stainless steel wall of the back-up design.

5.2. Cyclic thermal stresses of graphite armour tiles

Cyclic thermal stresses in a passively cooled graphite tile first wall were analysed for conditions of 1.1×10^6 normal 100-s burn cycles and 1908 plasma disruptions. The thermal analysis is presented in Section 4.3 and detailed stress analyses are presented in Ref.[4].

Initial analyses were based on the mechanical and physical properties with and without irradiation of a near-isotropic form of graphite, i.e. grade H451 nuclear graphite. Bulk damage and irradiation properties were assumed to be equivalent to those corresponding to a fission fast-neutron fluence of 6.3×10^{25} n/m^2. The total erosion of the tiles over the lifetime of the facility is about 3 cm. Therefore, if the end-of-life thickness required for structural support of the mechanical loads is 2 cm, the initial tile thickness must be 5 cm. Mechanical loading is primarily due to radially inward acting electromagnetic forces imposed during plasma disruptions.

Thermal stress analyses were performed for the INTOR reference surface heat flux and the high heat flux conditions of 11.6 W/cm^2 and 22.0 W/cm^2, respectively. The results show that raising the surface heat flux to 22.0 W/cm^2 has little impact on the tiles. Nearly doubling the surface heat flux slightly increases the thermal strain, with little change in thermal stresses. Even though the properties change considerably with irradiation, the thermal stresses are of the same magnitude for both irradiated and unirradiated tiles. The thermal stress range is small over the burn cycle when the tile edges are allowed to rotate, which greatly enhances the life of the tiles. The external restraint from the rails and the thermal stresses in the tiles are minimized by holding the tiles near the corners so that the tiles can freely deflect to a spherical shape due to the thermal gradient through the thickness. Thermal stresses near the support rails become excessive if the tiles and the actively cooled support rails are in intimate contact. Thermal gradients near the corners are increased by the additional heat flowing through the attachments. An insulated (low-conductance) joint is required to hold the thermal stresses at acceptable values. The results of these analyses, which do not include radiation-induced volumetric changes, show that the combined stresses can be kept low and therefore the tile should last for the life of the facility. The life-limiting factors are erosion or bulk damage due to irradiation.

6. DISRUPTION ANALYSIS

6.1. Wall vaporization and melting

A hard plasma disruption within INTOR creates intense first-wall surface heating. The energy retained at this surface, i.e. the difference between the incident plasma energy and that transported away by conduction and convection, produces a rapid temperature rise and a subsequent change of the material phase. The consequence of this phase change is surface ablation.

A number of first-wall ablation models [2 – 5] have been developed by the countries participating in the INTOR study. These models differed in the degree of complexity employed to predict the coupled phenomena of surface vaporization and vaporized material transport. In order to gain a perspective of the model development effort of all INTOR participants, a qualitative overview of the different models is given. The most comprehensive attempt at modelling various aspects of the ablation process has been made by the USA [4]. This model predicts:

- wall melting
- non-equilibrium mass transfer at the melt/vapour interface
- the dynamics of vaporized first-wall material as it expands into the INTOR vacuum vessel.

The model employs:

- a solution of the energy equation for the first-wall material
- a modified kinetic theory of the phase-change relationship for the melt/vapour interface
- a solution of the continuum fluid conservation equations of mass, momentum and energy.

Since good agreement has been obtained between the results of this model and those of other models recently developed, Sections 6.1.2 to 6.1.6 focus primarily on the features of the U.S. model and the results obtained for first-wall materials of stainless steel and carbon.

6.1.1. Overview of proposed INTOR first-wall ablation models

The earlier ablation models assumed a first-wall surface pressure [2 – 5], on the basis of which a surface vaporization temperature was determined through pressure/temperature saturation relationships. Once the surface temperature, as predicted by an analytical solution of the conduction equation, reaches the vaporization value, the surface is vaporized at a rate which maintains this temperature according to an energy balance at the wall surface. As an alternative to this approach, the ablation model discussed in Ref. [5] used one-dimensional

compressible steady-flow relationships to determine the surface vaporization temperature. With the surface pressure being defined through a compressible flow stagnation relationship and an assumed vapour pressure near the surface, the vaporization temperature was derived by equating the choked surface mass flow to that which could be generated according to the incident plasma energy and the latent heat of vaporization.

The more recent models [2, 3, 5] predict surface vaporization by neglecting the influence of the vapour pressure near the surface. The rate of surface vaporization is determined from a coupled solution of the conduction equation, modified to reflect a melt layer, and formulas which describe either the kinetics of evaporation or surface choking. The required surface pressure is obtained from saturation relationships and the predicted surface temperature. Such models are valid, provided the actual vapour pressure near the surface is less than that obtained from equations for choked compressible flow where the surface pressure becomes the stagnation pressure. It would appear that, for the range of plasma energies investigated so far, this is indeed the case, since excellent agreement has been obtained between the vaporization depth and melt-layer thickness predictions of these models and those of the U.S. model which attempts to predict the vapour pressure near the wall surface.

6.1.2. First-wall thermal model

During a plasma disruption, the first wall is subjected to intense surface heating. The energy retained at this surface, i.e. the difference between the incident plasma energy and that transported away by conduction and convection, results in a rapid temperature rise and a subsequent change of material phase. To account for the desired change-of-state processes, the retained energy of the first-wall material must be predicted both in time and space. This prediction was accomplished by a solution of the energy equation for the first-wall material. This equation was solved, in finite difference form, implicitly with equations of state that relate temperature and thermal conductivity to the predicted material energy.

The first-wall model was one-dimensional in nodal structure, and care was taken to provide adequate thermal detail in the regions where melting and vaporization were anticipated to occur. As vaporization proceeded, the node network was explicitly restructured to reflect the loss of material and a moving boundary.

6.1.3. Vacuum vessel vapour dynamics model

The rate of first-wall sublimation or vaporization depends not only on the level of retained energy at the surface of this wall but also on the dynamics of

the vapour phase adjacent to this surface. In particular, the transient vapour properties of pressure, density and energy must be predicted as this vapour stream expands into the INTOR vacuum vessel. These predictions were accomplished with the aid of a computer code which solves the one-dimensional continuum fluid conservation equations of mass, momentum and energy. The equation of state, relating density to pressure and energy, was taken as that of an ideal gas for this model.

6.1.4. First-wall surface vaporization model

The first-wall thermal model (Section 6.1.2) and the vacuum vessel vapour dynamics model (Section 6.1.3) are connected through the necessity of accounting for vaporization in the boundary conditions of both models. Vaporization was allowed to proceed either in a non-equilibrium mode at the first-wall surface/vapour interface or in equilibrium, as desired. The equilibrium vaporization model was primarily used as a check case for the non-equilibrium prediction. Non-equilibrium vaporization or sublimation was modelled by the modified kinetic theory phase-change relationship proposed by Schrage [26]:

$$j = \left(\frac{M}{2\pi R}\right)^{1/2} \left[\Gamma \sigma_c \frac{P_v}{T_v^{1/2}} - \sigma_e \frac{P_s}{T_s^{1/2}}\right]$$

where

j	=	vaporization mass flux ($kg/m^2 \cdot s$)
M	=	vapour molecular weight (kg/mole)
$P_{v,s}$	=	vapour pressure (N/m^2), first-wall surface
$T_{v,s}$	=	vapour temperature (K), first-wall surface
R	=	universal gas constant ($J/kg \cdot mole \cdot K$)
Γ, σ_c, σ_e	=	condensation or evaporation multipliers.

This relationship is based upon the assumption that the mass rate of flow (molecular flux) passing in either direction (to the right or to the left) through an imaginary plane is given by

$$|j| = \left(\frac{M}{2\pi R}\right)^{1/2} \frac{P}{T^{1/2}}$$

The Schrage relationship predicts the net flow through the vapour/liquid interface (i.e. $j_v - j_s$), with the two components of flow (j_v and j_s) being modified to compensate for non-ideal condensation or vaporization and for a superimposed

net vapour motion, Γ, towards or away from the surface, on the assumed Maxwellian distribution. The pressures and temperatures of this relationship are those which exist at several mean free paths from the evaporating surface. For this model they were taken as those of the first fluid computational cell (5 mm from the first wall), while those of the surface were taken as saturated values at the predicted surface energy. The coefficients of vaporization and condensation were taken as unity, and the Mach number correction coefficient (Γ) was determined from equations given in Ref.[26].

The boundary condition for the first-wall thermal model was an imposed surface heat flux, equal to the difference between the incident plasma flux and that carried away in the vaporized stream. The heat flux convected away in the vaporized stream was defined as the product of the vaporization mass flux and the heat of vaporization or sublimation. The imposed boundary condition for the momentum equation of the vacuum vessel vapour dynamics model is the surface vapour velocity, defined as the vaporization mass flux divided by the surface vapour density.

The equilibrium vaporization model assumed a pressure equilibrium between the first fluid computational cell and the surface of the first wall. With this pressure, which was used as a boundary condition for the first-wall thermal model, the surface temperature was obtained through saturation relationships. The imposed boundary condition for the momentum equation is the surface vapour velocity defined above. The rate of vaporization was specified to be the evaporative heat flux divided by the heat of vaporization. This heat flux was the difference between the incident plasma energy and that transported away from the surface by conduction. An upper limit on the surface vapour velocity for this model was the sonic velocity of an ideal gas at the surface conditions. If the velocity as predicted from the surface vaporization rate exceeded the sonic limit, the surface temperature and the surface pressure were re-evaluated to obtain the required heat flux balance for choke flow conditions.

6.1.5. Equations of state

Equations of state were obtained from the literature or developed from data in the literature [27, 28] for Type 316 stainless steel, beryllium and graphite. Analytical expressions for enthalpy as a function of temperature were developed, of the general form $E = a + bT + cT^2$, where E is the enthalpy in J/kg, T is the temperature in degrees kelvin, and a, b, c are constants. Expressions for vapour pressure as a function of temperature were fit, with the general form $\log_{10} P = d + f/T$, where P is the saturated vapour pressure in N/m^2 at temperature T, and d and f are constants.

TABLE VII-19. RESULTS (at 20 ms) OF THE NON-EQUILIBRIUM VAPORIZATION MODEL FOR VARIOUS DISRUPTION ENERGY DENSITIES

Energy density (J/cm^2)	First-wall surface temperature (K)	First-wall surface pressure (N/m^2)	Vapour pressure (N/m^2)	Vaporization depth (m)	Melt-layer thickness (m)
Carbon					
200	3030.5	1.92×10^{1}	6.32	6.08×10^{-9}	–
220	3208.8	9.76×10^{1}	3.17×10^{1}	2.96×10^{-8}	–
250	3440.4	6.27×10^{2}	2.03×10^{2}	1.97×10^{-7}	–
289	3646.8	2.70×10^{3}	8.79×10^{3}	1.19×10^{-6}	–
356	3774.4	6.17×10^{3}	2.02×10^{3}	4.96×10^{-6}	–
422	3841.1	9.27×10^{3}	3.40×10^{3}	9.96×10^{-6}	–
SS-316					
200	1937.5	2.28×10^{1}	7.82	3.40×10^{-9}	4.40×10^{-5}
220	2088.4	1.20×10^{2}	4.12×10^{1}	1.89×10^{-8}	7.01×10^{-5}
250	2290.4	7.59×10^{2}	2.66×10^{2}	1.25×10^{-7}	1.04×10^{-4}
289	2515.4	4.14×10^{3}	1.47×10^{3}	8.00×10^{-7}	1.40×10^{-4}
356	2727.3	1.58×10^{4}	5.71×10^{3}	4.75×10^{-6}	1.80×10^{-4}
422	2832.0	2.85×10^{4}	1.07×10^{4}	1.15×10^{-5}	2.05×10^{-4}

TABLE VII-20. COMPARISON OF NON-EQUILIBRIUM AND EQUILIBRIUM VAPORIZATION MODELS (at 20 ms) FOR A DISRUPTION ENERGY DENSITY OF 289.0 J/cm^2

Vaporization model	First-wall surface temperature (K)	Vaporization depth (m)	Melt-layer thickness (m)
Carbon			
Non-equilibrium	3646.8	1.2×10^{-6}	–
Equilibrium	3442.9	2.4×10^{-6}	–
SS-316			
Non-equilibrium	2515.4	8.0×10^{-7}	1.40×10^{-4}
Equilibrium	2353.2	1.01×10^{-6}	1.20×10^{-4}

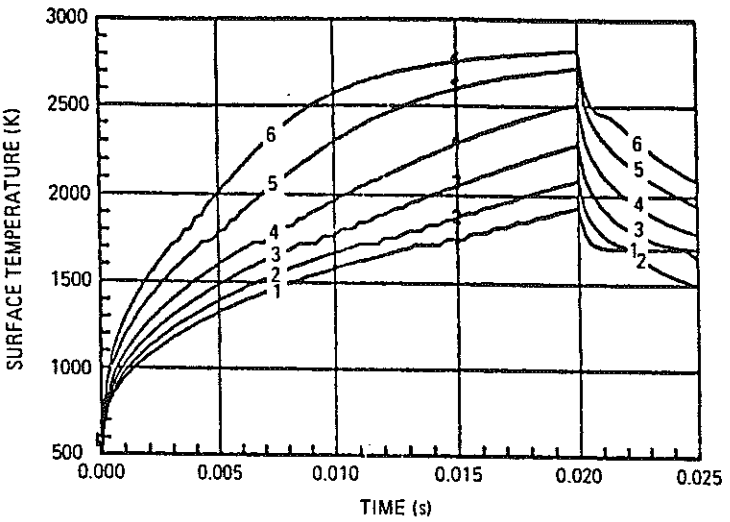

FIG. VII-17. Surface temperature history of stainless steel for a 20-ms disruption at deposited energy densities of: (1) 200 J/cm², (2) 220 J/cm², (3) 250 J/cm², (4) 289 J/cm², (5) 356 J/cm², (6) 422 J/cm².

6.1.6. Results

Tables VII-19 and VII-20 and Fig.VII-17 summarize the results obtained. The figure shows the predicted temperature response of the stainless steel first wall subjected to various plasma energy densities. The values for the various parameters, which were obtained from the non-equilibrium model, tend to converge at higher energy densities. This characteristic suggests that an increased fraction of the incident energy contributes to vaporization. Table VII-19 gives the predicted surface temperature, surface pressure, vaporization depth, melt-layer thickness, and vapour pressure near the first wall as a function of deposited energy density for graphite and stainless steel first walls.

A comparison of the predictions made with the non-equilibrium vaporization model and the equilibrium vaporization model is given in Table VII-20. These results indicate minor differences in the predictions of the two models. Since the equilibrium model continually encountered sonic-limited surface conditions, the predictions suggest an upper bound on the vaporization that can be expected from the non-equilibrium model.

6.2. Electromagnetic loading and melt-layer behaviour

6.2.1. Electromagnetic loading

When plasma disruptions occur, a toroidal current is induced in the first wall and blanket, tending to maintain the field formerly produced by the plasma.

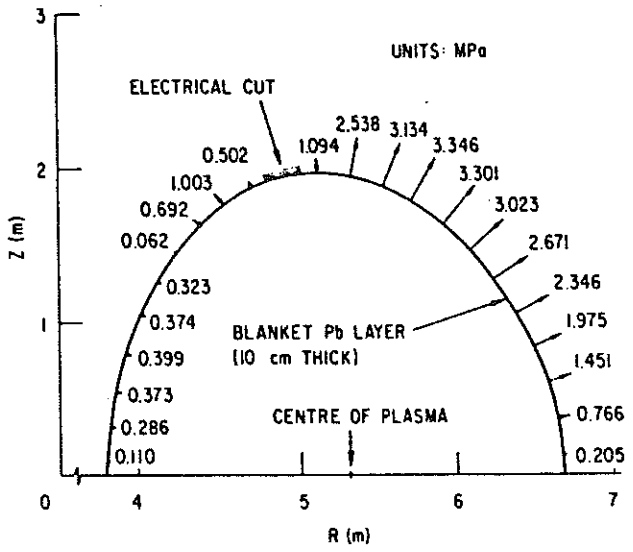

FIG. VII-18. Poloidal distribution of electromagnetic forces at 30 ms, for a lead blanket with two poloidal segments.

For an electrically continuous blanket, the current is strictly toroidal and does not interact with the toroidal field. However, if the blanket is segmented toroidally, radial and poloidal eddy-current components can interact with the toroidal field to produce large forces on the first wall and blanket. The magnitude of the force depends on the blanket material and thickness and on how finely the blanket is segmented toroidally and poloidally. In all cases a disruption time of 20 ms is assumed for the plasma current. Under suitable assumptions [2], an aluminium blanket, 26 cm thick and divided into 18 segments toroidally and 15 segments poloidally, experiences a peak force per unit area of 40.6 MPa. Similarly, under suitable assumptions [3], a lead blanket, 10 cm thick and divided into 24 segments toroidally, experiences a peak force per unit area of 5.8 MPa, 3.35 MPa or 2.56 MPa, if it has respectively zero, two or five segments poloidally. The two-segment case is closest to the actual design. Figure VII-18 shows the force distribution resulting from the two-segment case.

A first wall consisting of toroidally oriented tubes of aluminium or stainless steel, with an inner diameter of 2.0 cm and an outer diameter of 7.0 cm (aluminium) or of 3.6 cm (stainless steel), under suitable assumptions [4], experiences a peak force per unit area of 0.183 MPa (aluminium) or 0.065 MPa (stainless steel).

The results for all the above analyses are summarized in Table VII-21, which also gives the quantity $\rho F/A\delta$, which is a convenient measure for comparing the different results according to thickness and resistivity. The values of $\rho F/A\delta$ for

TABLE VII-21. PEAK ELECTROMAGNETIC FORCES ON BLANKET OR TUBULAR FIRST WALL DURING A PLASMA DISRUPTION

Case	Thickness, δ (m)	Resistivity, ρ ($\mu\Omega \cdot$m)	Peak force per area, F/A (MPa)	$\rho F/A\delta$ ($\Omega \cdot$Pa)	Ref.
Aluminium blanket	0.26	0.067	40.6	10.5	[2]
Lead blanket	0.10	0.31	3.35	10.4	[3]
Aluminium first wall	0.07	0.048	0.183	0.125	[4]
Stainless steel first wall	0.036	0.76	0.065	1.37	[4]

the two blanket analyses show remarkable (indeed fortuitous) agreement. The value for the stainless steel first wall is lower than the values for the blankets because only part of the induced current flows in the first wall and because the toroidal current in the first wall interacts only with the poloidal field. The value for the aluminium first wall is lower than the value for stainless steel because the eddy currents flow in one direction at one side of the tube and in the opposite direction at the other side; the resulting forces nearly cancel each other.

6.2.2. Melt-layer behaviour

Within the first few milliseconds of the disruption (i.e. before melting has begun) the current is uniformly distributed throughout the stainless steel first wall, so that the current in the melted layer is proportional to its thickness. The toroidally induced current interacts with the decreasing field from the plasma and the unchanging field from the PF coils to give a force which is initially into the plasma but which later reverses sign. Analysis [4] shows the force to be a maximum (275 Pa) at 5 ms and to reverse at 12 ms. Figure VII-19 shows the motion of particles subjected to that normal force, starting at 5 ms, 7 ms and 9 ms after the initiation of plasma current decay. The figure can be taken to represent an upper limit on the perpendicular motion of the melted layer, ignoring cohesive forces. Of course, if a portion of the melted layer breaks free under the action of the magnetic force, it will no longer carry a current and will, in this simple model, continue to move with constant velocity.

The motion of a melted layer along the wall has also been assessed [5]. The field lines are assumed to be at an angle of 30° with the first wall. (An angle of 45° approximately doubles the calculated displacement.) In this case it is

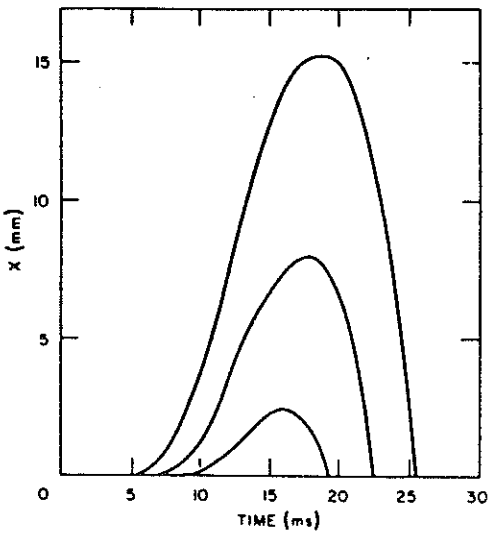

FIG. VII-19. Equivalent projectile motion under the force experienced by a particle in the melt layer, starting at 5 ms, 7 ms and 9 ms.

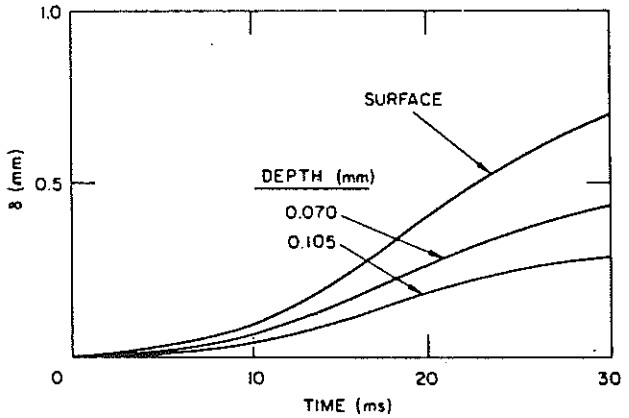

FIG. VII-20. Displacement of liquid film layers versus time.

possible to neglect forces of surface tension and to consider the force of reactive pressure to be equal at all the surface points. Film deceleration by forces of viscous friction was taken into account. Figure VII-20 shows the film displacement versus time for the various layers. The maximum displacement of a liquid film at 20 ms is 0.4 mm. After the end of a disruption the film re-solidifies. During this time, the film is decelerated by the field and forces of viscous friction. The maximum film displacement after the end of a disruption is 0.4 mm. Thus, the total film displacement does not exceed 0.8 mm.

The calculated displacements in these two analyses differ by more than an order of magnitude. Part of the difference arises because viscous forces were incorporated in the analysis of motion along the plate, while surface tension and other cohesive forces were neglected in the analysis of motion normal to the plate. Differences also arise because the field component producing a force along the plate is smaller than the component producing a normal force.

When an appropriate uncertainty is attributed to the results, neither analysis unequivocally provides an answer to the question of melt-layer stability. Further analytical and experimental efforts are definitely required to resolve this question.

7. LIFETIME ANALYSES

A major objective of the INTOR first-wall design study was to develop a first-wall design concept that could potentially last for the projected lifetime of the reactor. Based on the specified operating conditions and suggested design criteria, materials assessment and neutronics, thermohydraulics and stress analyses have been conducted to evaluate the performance of the proposed design concept. Significant uncertainties exist in the projected operating conditions, the materials data base, and the lifetime analyses. However, in most cases, substantial conservatism has been incorporated into the study to provide a reasonable degree of confidence that the design goal is attainable. Should the assumed operating conditions change significantly or the materials data base prove invalid, changes in the lifetime estimates or design concept may be warranted.

Erosion rates considered in specifying the thickness of the first wall include physical sputtering by charge-exchange neutrals, vaporization and melting of the wall during a plasma disruption, and coolant corrosion. The predicted erosion rates of the various regions of the first wall are summarized in Table VII-22 for each stage of operation. The major contribution to erosion is from physical sputtering on all regions during the burn. The base-line sputtering data (mono-energetic particles with normal incidence) are believed to be valid within a factor of ~ 1.5. The major uncertainties relate to the plasma edge conditions, i.e. edge energy, particle flux and angle of incidence. The proposed edge energy of 200 eV contains some conservatism. The calculations indicate that only modest vaporization occurs for the 20 ms reference disruption condition with 289 J/cm^2 of deposited energy density. This value assumes that nearly all of the plasma energy goes to the inboard wall (30% of total area) and that some regions receive twice the average value. The calculations indicate that a significant increase in energy deposition or a decrease in disruption time will lead to much larger erosion rates. However, conservatism is incorporated in the erosion allowance by assuming that all disruptions occur under the standard operating conditions

TABLE VII-22. EROSION (in mm) OF INTOR FIRST-WALL SYSTEM[a,b]

	Stages			Lifetime
	I	II	III	
Outboard wall and ripple armour region				
Physical sputtering (burn)	0.6	1.6	6.5	8.7
Limiter region				
Physical sputtering (burn)	0.6	1.6	6.5	8.7
Physical sputtering (start-up)	0.1	0.2	0.8	1.1
Total erosion	0.7	1.8	7.3	9.8
Inboard wall and beam shine-through region				
Physical sputtering (burn)	0.6	1.6	6.5	8.7
Vaporization during disruption	0.8[c]	0.2[c]	0.8[c]	1.8[c]
Total erosion	1.4	1.8	7.3	10.5

[a] Analyses indicate that blistering erosion and water corrosion are negligible.
[b] Surface melt layer predicted to form during a disruption is assumed not to erode.
[c] Allowance is twice the calculated value.

and peak on the same parts of the first wall, and no re-deposition on these parts occurs after disruption. Also, the vaporization allowance is twice the calculated value [4]. The major uncertainty involves the stability of the melt layer that is predicted to form during a disruption. Although the calculated forces on the melt layer are quite small and the region is molten for only a short time ($\sim$ 25 ms at the surface, with much of the melt layer molten for a shorter time), the present analyses are inadequate to demonstrate that the entire melt layer is stable. Additional analyses and experimental measurements are needed.

The thermohydraulic analyses indicate that the stainless steel wall temperatures during normal operation are well within the specified limit of 350°C. This temperature is generally considered to be a conservative operating limit for stainless steel. The irradiation data base is limited for the fusion reactor environment, but the available information does not indicate an unacceptable performance for the fluences and operating temperatures proposed. Swelling does not appear to be excessive at the relatively low operating temperatures. Loss of ductility is a major concern since limited data are available for the low-temperature range.

The establishment of criteria for specifying the minimum allowable ductility is an important issue. In general, the stress calculations have assumed the worst case for radiation creep, i.e. zero creep or complete relaxation at the burn conditions. The more likely intermediate cases should be less severe.

The stress analyses are based on data for mechanical properties without irradiation (see Table VII-18). Effects of the chemical and irradiation environments have not been taken directly into account. Also, property changes caused by mechanical work hardening or softening, or thermal effects have not been considered. However, the analyses are based on ASME code case criteria, which incorporate considerable conservatism. The use of cold-worked material provides a substantial margin in the allowable stress. However, more detailed stress analyses of constrained regions should be performed. Also, effects of weld regions and melting during disruptions have been neglected. In general, the fatigue life is based on thermal stresses that are predicted for the full wall thickness during the entire lifetime. Any thinning, caused for example by sputtering, should reduce the thermal stresses and, hence, increase the lifetime. If subsequent information indicates that the erosion rates are higher than those predicted, thinner walls with inherently longer fatigue lives could be used.
A major concern regarding the fatigue behaviour of the first wall relates to the possibility of stress corrosion cracking of the stainless steel wall in water, particularly since cold-worked material is proposed. However, coolant chemistry should be more easily controlled in the low-temperature, low-pressure water than in most other practical systems, e.g. steam generators.

The conservatism incorporated into the lifetime predictions is believed to be adequate to allow for uncertainties in the data base and the analyses. There is high confidence that the proposed first-wall concept will provide an acceptable design, though possibly not for the full reactor lifetime if the operating conditions are somewhat more severe than the reference values assumed. A short erosion life is only one reason for the design requirement that the first wall be replaceable, and it should be noted that this requirement arises mainly because of the possibility of a catastrophic failure of the first wall.

8. MECHANICAL DESIGN

The components of the first-wall system are listed in Section 1.

A major objective of the present study was to develop a first-wall design concept that could potentially last for the 15-year INTOR lifetime under the projected operating conditions. The proposed INTOR operating scenario and first-wall operating parameters are summarized in Tables VII-1 and VII-2.
In addition to the materials data-base assessment, the analyses conducted in the development of the reference first-wall system design concept include: neutronics,

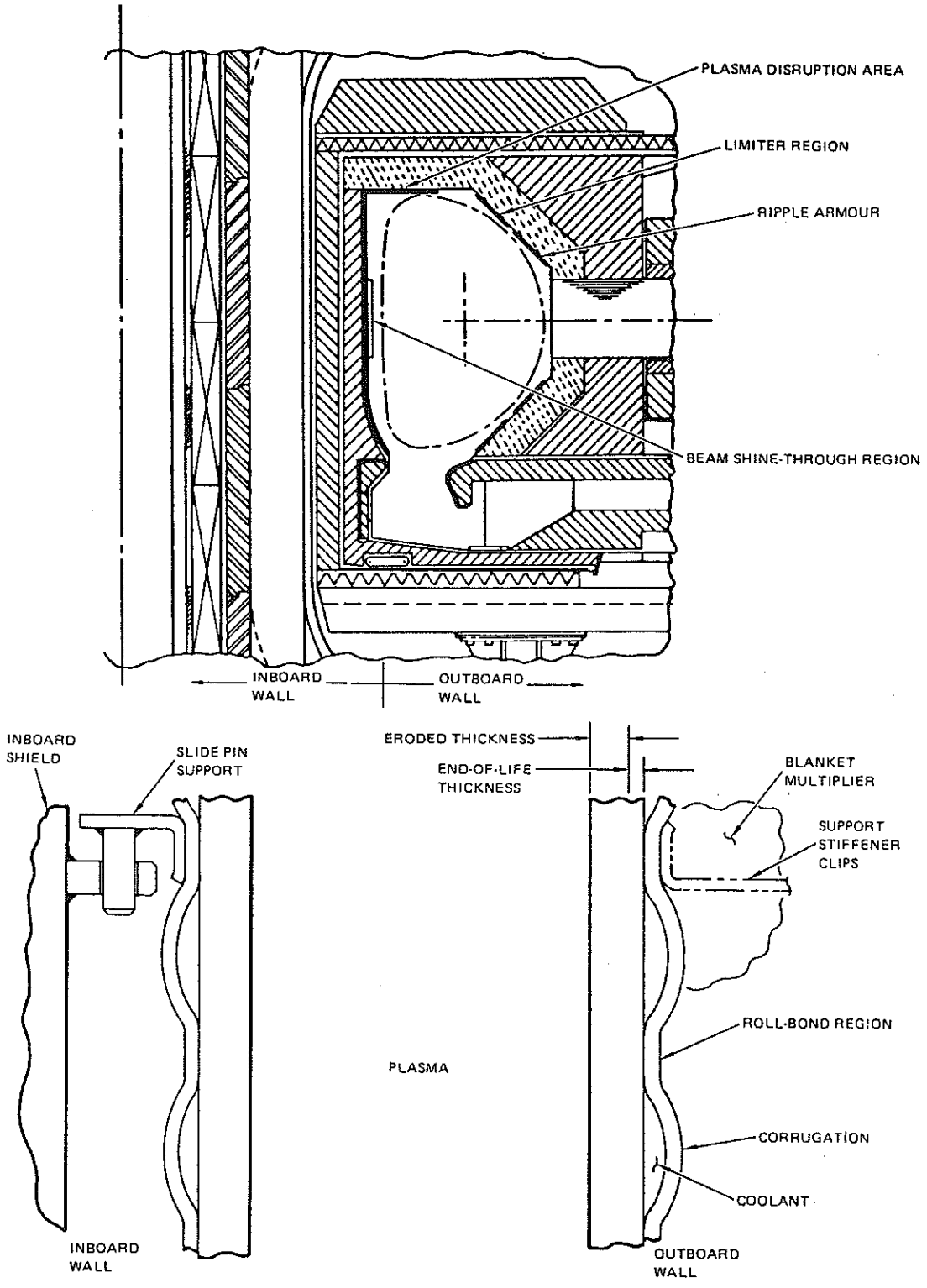

FIG. VII-21. First-wall configuration.

TABLE VII-23. DESIGN SPECIFICATIONS FOR REFERENCE FIRST-WALL CONCEPT

Water-cooled stainless steel panel
Water coolant (D_2O)
structure is maintained at low temperature
low pressure minimizes stress requirements
20% cold-worked Type 316 stainless steel
better radiation damage resistance
higher allowable stress
Panel-type construction
ease of fabrication
corrugated coolant channels minimize stress
longer lifetime than for construction with tubes
Outboard wall integral with blanket
minimizes structure and coolant (improved breeding)
serves as containment for neutron multiplier
ease of manifolding and support

thermohydraulics, stress and plasma disruption response. The first-wall design concepts considered in the present study include: (a) a water-cooled bare stainless steel wall, (b) a water-cooled bare aluminium wall, (c) a radiatively cooled graphite liner on the inboard wall, and (d) a low-Z (beryllium) coated (cladded) water-cooled stainless steel wall. Both tube-bank construction and various panel-type water-cooled wall concepts were considered. Grooved panels, both of stainless steel and aluminium, were considered as a means of reducing the thermal stresses in the concepts using thick metal walls. The general design philosophy for the special first-wall regions, i.e. the limiter, ripple armour and beam shine-through regions, was to incorporate them, if possible, in the normal first wall.

8.1. Reference first-wall design

A poloidal view of the reference reactor design, indicating the location of the first-wall system, i.e. the outboard wall, inboard wall, limiter region, beam shine-through region and ripple armour region, is shown in Fig.VII-1. All first-wall components are fabricated from 20% cold-worked Type 316 stainless steel and utilize low-pressure (< 1 MPa) water coolant. Figure VII-21 is a schematic diagram

of the panel-type construction, showing the thicker flat panel that faces the plasma and the corrugated back-panel that forms the coolant channels. The two panels are diffusion-bonded together and the welded supports are spaced as required. The thickness of the plasma side-panel is sufficient to withstand the sputtering and vaporization erosion predicted for the full lifetime of the reactor. The special regions are a part of the first wall, with minor thickness modifications to allow for effects caused by the preferential heat or particle fluxes.

Table VII-23 summarizes the design specifications for the reference first-wall design. The low-temperature water coolant maintains the structure at low temperature, which provides acceptable structural properties under irradiation. The low pressure also tends to minimize primary stress requirements. The 20% cold-worked stainless steel is selected because of superior radiation damage resistance and the higher allowable design stress. The panel-type construction is proposed because of ease of fabrication, reduced stresses resulting from the thin corrugated coolant channels, and a longer predicted lifetime than for tube-bank designs. The outboard wall is an integral part of the blanket and serves as the containment for the neutron multiplier. This tends to minimize structure and coolant volumes between the plasma and the breeder zone, which enhances the breeding performance. The manifolding and support structures are readily incorporated in the blanket.

The resistance-weld method used to bond sheets together between channels is believed to cause a minimal impact on the radiation damage resistance of the structural material. Examination of the weld zone of resistance-welded material shows that the microstructure is not markedly changed in the weld area. Since the microstructure is important for radiation damage resistance and for maintaining the properties of the cold-worked material, the roll-bonding process is believed to be a good method for first-wall fabrication. Any separation or cracking of welds between channels results only in a minute passage of coolant between adjacent channels. This is not significant since the flow is in the same direction across the first wall for all channels. The probability of a leak through a front or rear sheet to the plasma region or to the multiplier region is considered to be very low. The corrugated panels are configured into a first wall such that the coolant flow is vertical on the inner leg of the sector and horizontal (across the width of the sector) in the outer and upper areas of the first wall.

In the outboard region, the first wall is an integral part of the blanket. Support for both the first wall and multiplier is provided by stiffening flanges between the first and second wall. These supports are provided by locally roll-bonding stiffening flanges to the corrugated sheets. The first wall provides sufficient cooling for both the first wall and multiplier, which results in a total heat load equivalent of $\sim 60\ W/cm^2$ when accounting for the surface heat flux ($13\ W/cm^2$), nuclear heating in the first wall ($15\ W/cm^2$), and nuclear heating in the multiplier ($\sim 32\ W/cm^2$). These combined heat loads result in a 50°C

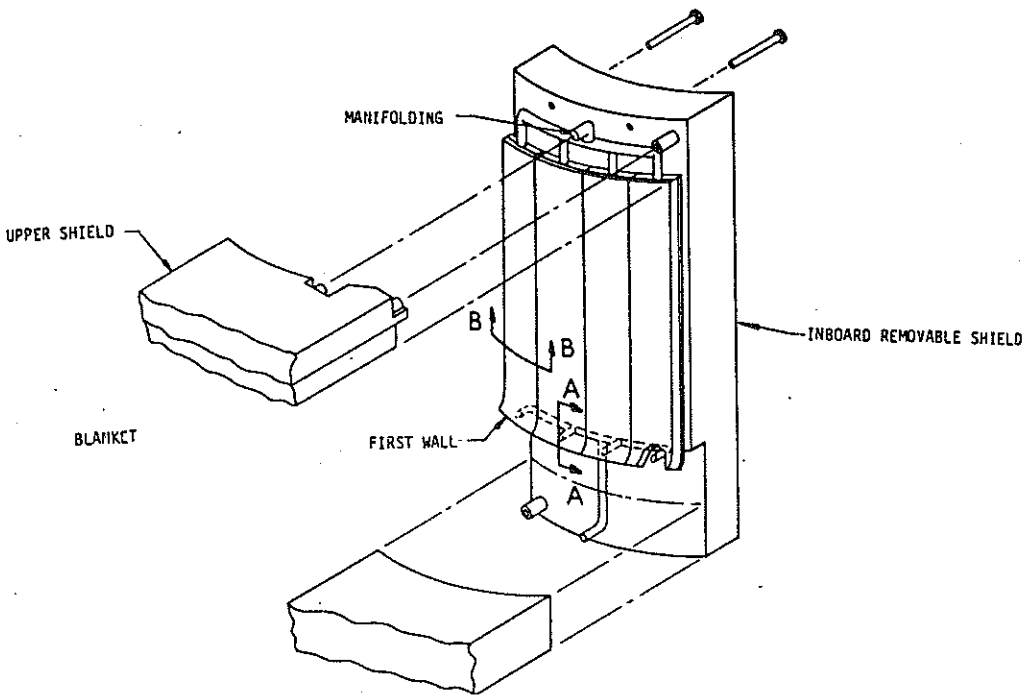

FIG. VII-22. Inboard wall configuration.

temperature rise as the coolant flows at 3 m/s through the cooling passages. The effective coolant thickness is 0.3 cm.

The first wall located at the inboard shield is made as an integral part of the shield which is removed with the first-wall shield sector. This portion of the shield is 45 cm thick, is made of Type 316 stainless steel and incorporates 10% water for cooling. The first-wall configuration is shown in Fig.VII-22. It is divided into 30-cm-wide strips that span ~ 4 m from an inlet manifold near the divertor throat to the top of the shield sector. The 30 cm width of the panel strips is determined by the support structure required to withstand plasma disruption loads. Each narrow panel is firmly attached at the reactor mid-plane and the end-supports are slotted to permit a thermal growth of 0.4 cm during the burn cycle. The coolant flow required for the inboard panel is 4.5 kg/s to limit the temperature rise to 50°C. This results in a 15 cm^2 inlet manifold size (4.5 cm diameter) for the inner leg of each sector.

Replacement of the inboard first wall is not planned during the lifetime of the reactor, but the capability for it is provided. The outboard first wall is integral with the blanket, so a replacement can be made by replacing the blanket. The inboard wall is a part of the shield that is removed with the sector. In the event of a first-wall failure, the inner leg can be removed and replaced. Coolant inlet/outlet pipes are located at the top and bottom of the sector where access is provided for cutting and re-welding.

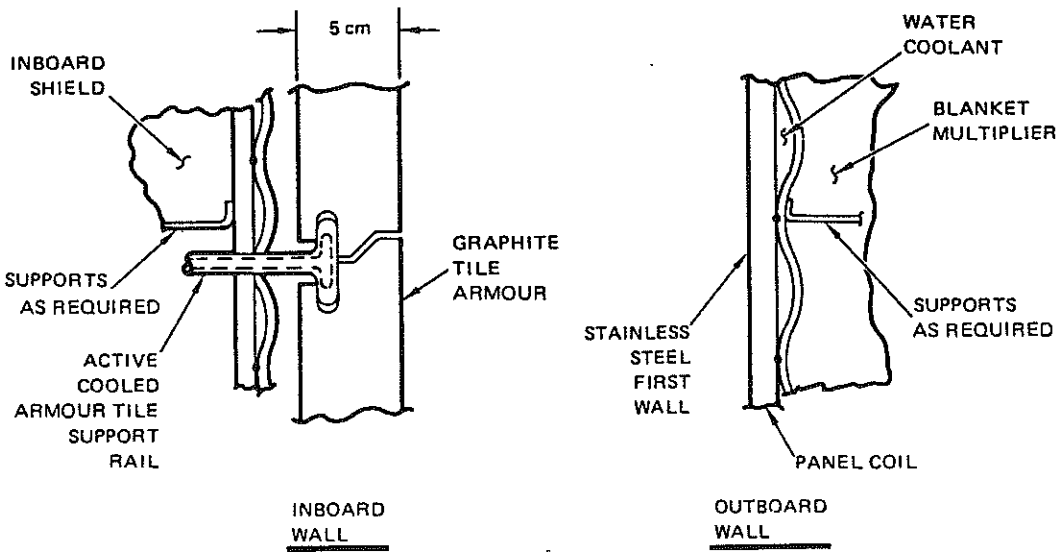

FIG. VII-23. Back-up design: graphite armour inboard wall and bare stainless steel outboard wall.

8.2. Back-up design

The back-up design is identical to the reference design, except that the plasma disruption area is lined with radiatively cooled graphite tiles. The graphite tiles chosen for this design are 4 cm thick by 30 cm square and cover 145 m^2. Nuclear heating in the tiles produces 50 MW of additional heat load that must be radiated to the outboard wall and to the wall behind the tiles. Maximum tile temperatures vary from ~ 200°C at the start of an equilibrium burn cycle to ~ 300°C at the end of the cycle.

The graphite tiles are eroded by vaporization when subjected to plasma disruptions, by chemical sputtering due to interaction with the plasma, and by physical sputtering caused by high-energy plasma particle impingement. Total erosion of the tiles over the lifetime of the reactor is 20 mm. In addition, 20 mm of graphite is required at the end of life to provide adequate structure in order to prevent cracking due to electromagnetic loads that occur during a plasma disruption. This results in a total required thickness of ~ 40 mm.

The carbon tiles are attached to actively cooled rails that are welded to the corrugated panel face. The rails are installed in segments to permit entry and exit of the coolant without excessive temperature rise. A sketch of the concept is shown in Fig. VII-23. The armour tiles are attached to the rails while the sector is removed from the reactor. The rails support the tiles at the corners but allow for some deflection to reduce the thermal stresses.

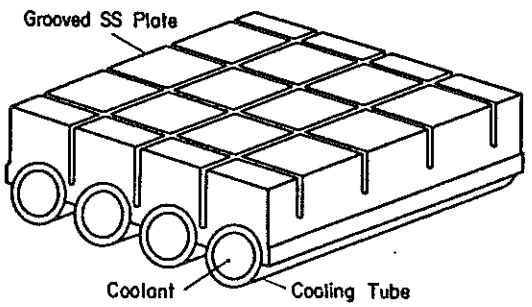

FIG. VII-24. First-wall concept with grooved structure.

The outboard wall is the same as in the reference design, except that it is subjected to a higher surface heat flux of ~ 28 W/cm^2, of which about 16 W/cm^2 results from the nuclear heat radiated from the graphite tiles. Lifetime analyses have shown that stress criteria and fatigue life can be met with the reference outboard wall design made from 20% cold-worked Type 316 stainless steel [4].

Concerns with the back-up design include:
- uncertainties in the chemical sputtering rate of graphite
- carbon deposition, for instance on cryosorption pump surfaces
- carbon embrittlement of structural materials
- complexity of attaching the graphite tiles.

8.3. Design options

8.3.1. Grooved wall

A grooved structural wall was investigated to determine if a thicker stainless steel wall could be used. The grooves should reduce thermal stresses by relieving constraints on the outer surface of the wall. The concept is shown schematically in Fig. VII-24. A local stress concentration at the grooves results (with a theoretical elastic stress concentration factor of 2 to 2.5). The stress concentration must be included in the allowable stresses in the wall caused by coolant pressure, plasma disruptions and thermal gradients. Since the stress at the notch is compressive, crack propagation will not occur. However, even if stress reversal would occur at the crack tip, analysis indicates that the crack propagation rates would be tolerable.

Analyses conducted for INTOR indicate that the grooved-wall concept permits the use of a thicker wall which will withstand higher erosion rates. The wall thickness can be increased until the maximum allowable structural temperature limit is reached. A typical grooved-wall panel incorporates grooves 1 mm wide × 1 cm deep, in a 10 cm grid.

TABLE VII-24. COMPARISON OF INTEGRAL AND SEPARATE FIRST-WALL CONCEPTS

	Integral	Separate
Breeding ratio	Higher by 10% (less steel, less water)	–
Vacuum surface area	380 m^2	1040 m^2
Thermal stress	Reduced by backside heating	–
Replacement	With blanket	Individual panel
Reliability	Improved (fewer pieces)	–
Fabrication	Simplified	–
Support method	Welding	Slide pins
Concerns	Replacement costs	Tritium costs Complexity Support

8.3.2. Wall configuration

A concept in which the first wall is an integral part of the blanket was selected for the outboard wall to enhance the tritium-breeding capability. The design choice is primarily a compromise between the cost of replacing a first-wall/blanket module in the event of a first-wall failure and the economic penalty associated with a loss of tritium-breeding capability if a separate first wall is used in front of the blanket. An integral design is generally simpler and results in an increase of the breeding ratio of about 0.1 because less metal is located in front of the breeder material. A comparison of the two concepts is given in Table VII-24. Since plasma disruptions do not tend to occur on the outboard wall, its failure rate should be low compared with that of the inboard wall. The integral wall is also easy to support and can serve to cool the multiplier.

A factor that must be considered in the selection of the integral first wall and blanket is the effect of the support on the thermal stresses. The two different design approaches [2, 5], which are shown in Fig. VII-25, include provisions for multiplier cooling. The first wall based on tubes is not constrained by the blanket, but it has a larger thickness. As a result, the back-sides of the tubes provide constraints that increase the total thermal stresses in the first wall. Slotted stiffeners are used in the panel design to permit longitudinal thermal growth, while lateral growth is permitted by the flexibility of the stiffeners to side-loads.

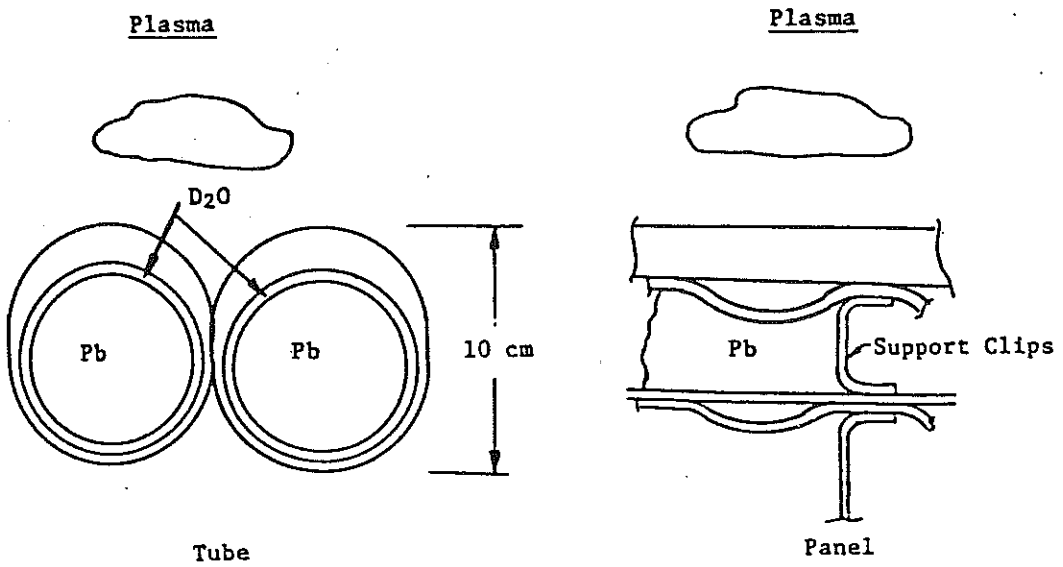

FIG. VII-25. Integral first-wall concepts.

In both designs, constraints at the edges require detailed investigation to minimize thermal stresses. The tubes can possibly be bent around the corner [2] to permit some stress relief; but in the panel design, the thin side-walls of the blanket module will provide some stress relief.

REFERENCES TO CHAPTER VII

[1] INTOR GROUP, International Tokamak Reactor: Zero Phase (Rep. Int. Tokamak Reactor Workshop Vienna, 1979), International Atomic Energy Agency, Vienna (1980) 650 pp. *See also:* Summary in Nucl. Fusion 20 3 (1980) 349.

[2] Euratom Conceptual Design Contribution to the INTOR Phase-One Workshop, Rep. Commission of the European Communities, Brussels (1981).

[3] Japanese Conceptual Design Contribution to the INTOR Phase-One Workshop, Rep. Japan Atomic Energy Research Institute, Tokai-mura (1981).

[4] USA Conceptual Design Contribution to the INTOR Phase-One Workshop, Rep. INTOR/81-1, Georgia Institute of Technology, Atlanta, GA (1981).

[5] USSR Conceptual Design Contribution to the INTOR Phase-One Workshop, Rep. Kurchatov Institute, Moscow (1981).

[6] ROTH, J., et al., Data on Low Energy Light Ion Sputtering, Rep. IPP-9/26, Max-Planck Institut für Plasmaphysik, Garching (1979).

[7] SMITH, D.L., J. Nucl. Mater. 75 (1978) 20; *see also:* Proc. Workshop on Sputtering caused by Plasma Surface Interaction, Argonne National Laboratory, IL, CONF-790775 (1979) 15–1.

[8] KAMINSKY, M., et al., Thin Solid Films 73 (1980) 91.

[9] ROTH, J., et al., J. Nucl. Mater. **85, 86** (1979) 1077.
[10] ROTH, J., et al., Plasma Wall Interactions, Pergamon Press, London (1977).
[11] BUSHAROV, N.P., GORBATOV, E.A., GUSEV, V.M., GUSEVA, M.I., MARTYNENKO, Y.V., J. Nucl. Mater. **63** (1975) 4772.
[12] LIU, G.N.-K., National Technical Information Service, Springfield, AD Rep. No. 779949/76A (1973).
[13] LOOK, G.W., BASKES, M.I., J. Nucl. Mater. **85, 86** (1979) 995.
[14] WILSON, K.L., THOMAS, G.J., BAUER, W., Nucl. Technol. **29** (1976) 322.
[15] BAUER, W., J. Nucl. Mater. **76, 77** (1978) 3.
[16] WIFFEN, F.W., "The influence of irradiation on the properties of Patch A alloy weldments", Alloy Development for Irradiation Performance, Quart. Prog. Rep. for Periods ending 30 Sep. 1979 (1979) 128, and 31 Dec. 1979 (1979) 28.
[17] GROSSBECK, M.L., MAZIASZ, P.J., J. Nucl. Mater. **85, 86** (1979) 883.
[18] AMERICAN SOCIETY OF MECHANICAL ENGINEERS, ASME Code Case 1592–10, Nuclear Components in Elevated Temperature Service (1977).
[19] GROSSBECK, M.L., LIU, K.C., "Low cycle fatigue behaviour of 20% cold-worked Type 316 stainless steel after irradiation in HFIR", Alloy Development for Irradiation Performance, Quart. Prog. Rep. for Period ending 30 June 1979 (1979) 42.
[20] MAZIASZ, P.J., GROSSBECK, M.L., "Swelling and microstructure of HFIR-irradiated 20%-cold-worked Type 316 + 0.23 wt.% Ti", Alloy Development for Irradiation Performance. Quart. Prog. Rep. for Period ending 31 Dec. 1980 (1981) 43.
[21] DRALEY, J.E., REUTHER, W.E., GREENBERG, S., Corrosion of some Reactor Materials in Dilute Phosphoric Acid, Argonne National Lab., IL, Rep. ANL-6206 (1961).
[22] EMMETT, M.B., The MORSE Monte Carlo Radiation Transport Code System, Oak Ridge National Lab., TN, Rep. ORNL-4972 (1975).
[23] ROUSSIN, R.W., et al., VITAMIN-C: The CTR Processed Multigroup Cross Section Library for Neutronics Studies, Oak Ridge National Lab. TN, Rep. ORNL/RSIC-37 (ENDF-296) (1980).
[24] GOHAR, Y., ABDOU, M.A., MACKLIB-IV: A Library of Nuclear Response Functions Generated with the MACK-IV Computer Program for ENDF/B-IV, Argonne National Lab., TN, Rep. ANL/FPP/TM-106 (1978).
[25] JUNG, J., A computational method for neutron transport problems in toroidal geometry, Nucl. Sci. Eng. **65** (1978) 130.
[26] SCHRAGE, R.W., A Theoretical Study of Interphase Mass Transfer, Columbia University Press (1953).
[27] CHOONG, S.K., Thermophysical Properties of Stainless Steels, Argonne National Lab., IL, Rep. ANL-75-55 (1975).
[28] HULTGREN, R., et al., Selected Values of the Thermodynamic Properties of the Elements, American Society for Metals, Metals Park, OH (1973).